

PAPER

Electrostatic interactions between ions near Thomas–Fermi substrates and the surface energy of ionic crystals at imperfect metals

V. Kaiser,^a J. Comtet,^a A. Niguès,^a A. Siria,^a B. Coasne^{*b} and L. Bocquet^{*a}

Received 19th December 2016, Accepted 27th January 2017

DOI: 10.1039/c6fd00256k

The electrostatic interaction between two charged particles is strongly modified in the vicinity of a metal. This situation is usually accounted for by the celebrated image charges approach, which was further extended to account for the electronic screening properties of the metal at the level of the Thomas–Fermi description. In this paper we build upon a previous approach [M. A. Vorotyntsev and A. A. Kornyshev, *Zh. Eksp. Teor. Fiz.*, 1980, **78**(3), 1008–1019] and successive works to calculate the 1-body and 2-body electrostatic energy of ions near a metal in terms of the Thomas–Fermi screening length. We propose workable approximations suitable for molecular simulations of ionic systems close to metallic walls. Furthermore, we use this framework to calculate analytically the electrostatic contribution to the surface energy of a one dimensional crystal at a metallic wall and its dependence on the Thomas–Fermi screening length. These calculations provide a simple interpretation for the surface energy in terms of image charges, which allows for an estimation of the interfacial properties in more complex situations of a disordered ionic liquid close to a metal surface. The counter-intuitive outcome is that electronic screening, as characterized by a molecular Thomas–Fermi length l_{TF} , profoundly affects the wetting of ionic systems close to a metal, in line with the recent experimental observation of capillary freezing of ionic liquids in metallic confinement.

1 Introduction

Room-temperature ionic liquids (RTILs)¹ are a class of materials with broad promise for energy storage² and nanolubrication.^{3,4} Physically, they are solventless electrolytes which remain liquid at room temperature, as the size of the constituent species competes with the Coulomb interaction to prevent

^aLaboratoire de Physique Statistique, Ecole Normale Supérieure, UMR CNRS 8550, PSL Research University, 75005 Paris Cedex 05, France. E-mail: lyderic.bocquet@ens.fr

^bLaboratoire Interdisciplinaire de Physique, CNRS and Université Grenoble Alpes, UMR CNRS 5588, 38000 Grenoble, France

1 crystallization. Electrostatic interactions make such systems strongly correlated,
even in the liquid phase,⁵ as highlighted by a number of specific properties
exhibited by RTILs, such as layering,^{6–9} crowding in the double layer,¹ and the
5 recently observed phenomena of long-range electrostatic interactions in RTILs¹⁰
and capillary freezing in confinement.¹¹ This points to the peculiar interfacial
properties of RTILs, many aspects of which remain puzzling and defy theoretical
understanding. Such properties are however extremely interesting for their
potential to be harnessed for various applications.^{12–17}

10 In the present paper, our aim is to explore the impact of the substrate elec-
tronic properties on the interfacial properties of RTILs. This is particularly
motivated by our recent experiments, highlighting the solidification of a RTIL in
confinement. This was interpreted in terms of capillary freezing at the nanoscale,
which is found to strongly increase as the conductivity of the substrate
15 increases.¹¹ These experiments point to the electronic properties of the substrate
having an impact on the phase and interfacial properties of RTILs, which remains
to be thoroughly rationalized.

Our goal is to set up the microscopic foundations to explore, *e.g.* by means of
molecular simulations, the interface between an ionic system and an imperfect
metallic substrate. The latter is modelled at the Thomas–Fermi (TF) level of theory
for electronic screening, which allows us to interpolate continuously between
20 insulators to ideal metals.¹⁸ Modelling of TF interfaces has drawn attention in the
context of metallic and semiconducting junctions^{48–50} and electrochemistry,
especially work functions involved in adsorption of charges and their configura-
tion at surfaces.⁴⁵ In particular we build on the pioneering work by Kornyshev
et al.^{19–21,43} who, in a series of papers, set up the framework to describe electro-
statics near TF walls, and even the two-dimensional crystallisation of charges
25 along the surface.^{45,46} Our objective is to obtain – here, at the level of the Laplace
estimate for interfacial tensions²² – an estimate of the electrostatic contribution to
the interfacial energy of an ionic crystal at a TF substrate, which extends outward
perpendicular to the surface.

We accordingly proceed in several steps: we first derive the analytical expres-
sions for the 1-body and 2-body electrostatic interactions between two ions close
35 to a TF substrate (Section 2 of the paper); we also propose further manageable and
versatile expressions for the interaction potential, in a form suitable for imple-
mentation in (future) molecular simulations; then using the proposed frame-
work, we calculate the surface energy of 1D, 2D, and 3D ionic crystals close to a TF
wall, as a function of the TF screening length (Section 3 of the paper). Our theory
40 predicts a lowering of the electrostatic energy of crystals due to the charge
induced in the substrate, with better conductors leading to better charge
screening and lower interfacial energy. We conclude with general perspectives
and extensions of the proposed framework in the context of a number of recent
experimental observations.

2 Electrostatics close to Thomas–Fermi surfaces

2.1 Thomas–Fermi screening and Green function

50 **Thomas–Fermi screening.** In electrostatics at the macroscale, any conductor is
seen as an idealized metal which perfectly screens any external charge at infinitely
short distances.²³ An external charge close to the ideal metal interface induces

1 a charge which is confined to the surface. The potential in the exterior of the
 metal can be expressed as a sum of the external-charge potential and the potential
 of an image charge of equal but opposite sign, mirrored by the surface. Unlike the
 surface charge, this image charge is purely a mathematical tool, as any real charge
 5 in an ideal metal is confined to the surface. The ideal metal limit has been treated
 in simulations by methods implementing the image charge method and its
 refinements in multiple fashions.^{24–26}

The perfect screening picture breaks down at the nanoscale as the screening
 charge cannot be localized due to the fundamental principles of quantum
 10 mechanics.²⁷ Delocalisation of the screening charge then results in screening at
 a finite wavelength for any external charge perturbing the system. The simplest
 screening theory, due to Thomas and Fermi, takes into account the competition
 between the energy gain due to screening of the external charge and the energy
 cost of localising the screening charge, while neglecting further correlations due
 15 to the wave-like nature of (quasi-)electrons.¹⁸

Electrostatics under vacuum or in an insulator next to the surface of
 a Thomas–Fermi (TF) metal (located in the half plane $z < 0$) follows the Poisson
 equation of electrostatics, stated here as a Green function problem for a point
 20 charge at $z = a$,

$$\Delta\psi_{\text{I}} = -\frac{Q\delta(z-a)\delta(R)}{2\pi\epsilon_0\epsilon_{\text{I}}R}, \quad (1)$$

and the Thomas–Fermi equation

$$\Delta\psi_{\text{II}} - \kappa_{\text{TF}}^2\psi_{\text{II}} = 0 \quad (2)$$

where the Thomas–Fermi wavevector $\kappa_{\text{TF}} = l_{\text{TF}}^{-1} = \sqrt{\epsilon\epsilon_{\text{II}}e^2\mathcal{D}(E_{\text{F}})}$ expresses the
 strength of the screening which increases with the density of states at the Fermi
 30 level $\mathcal{D}(E_{\text{F}})$ (in the zero-temperature approximation). Increased $\mathcal{D}(E_{\text{F}})$ permits
 the electron density to vary more with a lesser effect on the chemical potential of the
 local Fermi liquid, thus reducing the cost of localised screening, and reducing l_{TF} .

Green function of a charge close to a TF substrate. The Green function of
 a charge Q at distance a from the surface is central to the derivation of the
 potential energies and the thermodynamic properties under investigation. The
 35 configuration is shown in Fig. 1. The Poisson equation (1), and the TF equation (2)
 govern the electrostatic potential outside, and inside the TF metal, respectively.

The Green function can be calculated using the Hankel transform method.²⁸

The latter is defined as $\psi(z, K) = \int dRRJ_0(KR)\psi(z, R)$, where R is the radial
 40 component along the surface, and K the corresponding wavevector. Applying the
 Hankel transformation, the previous eqn (1) and (2) for the Green function read

$$(\partial_{zz} - K^2)\psi_{\text{I}} = -\frac{Q\delta(z-a)}{2\pi\epsilon_0\epsilon_{\text{I}}}, \quad (3)$$

$$(\partial_{zz} - \chi_{\text{TF}}^2)\psi_{\text{II}} = 0, \text{ where } \chi_{\text{TF}}^2 = K^2 + \kappa_{\text{TF}}^2. \quad (4)$$

Boundary conditions at the surface are given by the continuity of the potential
 50 $\psi_{\text{I}}(z = 0_+) = \psi_{\text{II}}(z = 0_-)$ and the electric displacement field $\epsilon_{\text{I}}[\partial_z\psi_{\text{I}}](z = 0_+) -$

1

5

10

15

20

25

30

35

40

45

50

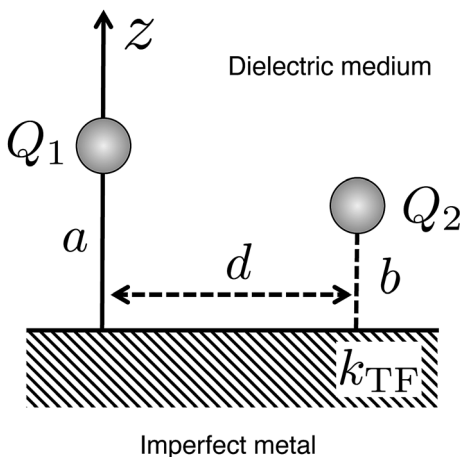


Fig. 1 Sketch of two charges close to a Thomas–Fermi metal.

$\varepsilon_{\text{II}}[\partial_z \psi_{\text{II}}](z = 0_-) = 0$. Moreover, the potential vanishes at infinity in all directions. The resulting Green function reads (as shown in various ways in ref. 19–21, 43, 48 and 50):

$$\psi_I^>(a|z > a, K) = \frac{Q}{4\pi\varepsilon_0\varepsilon_1 K} \left[e^{+Ka} + \frac{\varepsilon_1 K - \varepsilon_{\text{II}}\chi_{\text{TF}}}{\varepsilon_1 K + \varepsilon_{\text{II}}\chi_{\text{TF}}} e^{-Ka} \right] e^{-Kz} \quad (5)$$

$$\psi_I^<(a|z < a, K) = \frac{Q}{4\pi\varepsilon_0\varepsilon_1 K} \left[e^{+Kz} + \frac{\varepsilon_1 K - \varepsilon_{\text{II}}\chi_{\text{TF}}}{\varepsilon_1 K + \varepsilon_{\text{II}}\chi_{\text{TF}}} e^{-Kz} \right] e^{-Ka}$$

$$\psi_{\text{II}}(a|z, K) = \frac{Qe^{-Ka}}{4\pi\varepsilon_0\varepsilon_1 K} \frac{2\varepsilon_1 K}{\varepsilon_1 K + \varepsilon_{\text{II}}\chi_{\text{TF}}} e^{+\chi_{\text{TF}}z}, \quad (6)$$

where the first term in the brackets corresponds to the potential of the point external charge, while the other one to the response of the TF surface. Within the Thomas–Fermi framework, the physical induced charge is proportional to the potential in the metal

$$\rho_{\text{ind}}(a|z, K) = -\varepsilon_0\varepsilon_{\text{II}}\kappa_{\text{TF}}^2 \psi_{\text{II}}(a|z, K) = -\frac{\varepsilon_{\text{II}}\kappa_{\text{TF}}^2 Q e^{-Ka + \sqrt{K^2 + \kappa_{\text{TF}}^2}z}}{2\pi(\varepsilon_1 K + \varepsilon_{\text{II}}\sqrt{K^2 + \kappa_{\text{TF}}^2})} \quad (7)$$

which replaces the induced surface charge in the perfect metal case due to the finite screening length in the metal. In the Thomas–Fermi (TF) case, the induced charge is no longer confined to the surface but decays exponentially with the distance from it. As shown in ref. 19–21, one remarkable property is that the lateral extent of the screening cloud scales as $\varepsilon_1 l_{\text{TF}}/\varepsilon_{\text{II}}$. It can therefore spread out significantly in cases of a large dielectric contrast between the insulator and the conductor $\varepsilon_1 > \varepsilon_{\text{II}}$.

The full inversion of the Hankel transforms in terms of analytic functions is not analytically feasible. But they constitute a starting point for an approximation scheme. In the latter this allows us to express the single-body electrostatic energy in terms of simple integral expressions, and expand the two-body part in series in the Thomas–Fermi length l_{TF} . This expansion also yields new physical insights into the structure of these potentials, for example, that the Green function can be

expressed in terms of an image multipole expansion akin to the image charge expression for the ideal metal.

A numerical inversion of the potential and the induced charge distribution is also feasible, but not very efficient for simulation purposes where it needs to be repeated many times for each time step. Below, we therefore propose approximated forms for the associated electrostatic energy, which can be handled numerically.

2.2 One-body interaction: a single charge close to a TF surface

We start by considering a single, isolated particle close to a flat surface. In the case of an ideal metal, the potential of a charge can be found from the image charge method,²³ and the electrostatic energy $U_{\text{ideal}}^{(1)} = -Q^2/[16\pi\epsilon_I\epsilon_0a]$ is half of what an equivalent pair of real charges would yield.^{23,29}

The total electrostatic energy is half the scalar product of the charge density and the electrostatic potential, split between the induced charge (ρ_{ind} , $\psi_{\text{TF}} = \psi_{\text{II}}$, $z < 0$ support) and the external charge (ρ_{cr} , $\psi_{\text{cr}} = \psi_{\text{I}}$, $z > 0$ support) parts

$$\begin{aligned} U^{(1)}(a) &= \frac{1}{2} \int_{-\infty}^{+\infty} dz \int_0^{+\infty} 2\pi R dR \rho(a|z, R) \psi(a|z, R) \\ &= \pi \int_{-\infty}^{+\infty} dz \int_0^{+\infty} dK K [\rho_{\text{ind}}(a|z, K) + \rho_{\text{cr}}(a|z, K)] \psi(a|z, K) \end{aligned} \quad (8)$$

where we used the Plancherel theorem for the Hankel transform to equalize the direct and reciprocal space integrations. This expression can be used for TF metal and is equivalent to $\int_V \epsilon |\nabla\psi|^2/2$ because we treat the electrostatics of the system in the whole space and we have no explicit surface charges.²³

The resulting expressions for $U^{(1)}(a)$ are obtained in terms of an integral \mathcal{I}_{ext} over the dimensionless variable $\lambda = Ka$

$$U^{(1)}(a) = -\frac{Q^2}{16\pi\epsilon_0\epsilon_I a} (1 - \mathcal{I}_{\text{ext}} + \epsilon_I \mathcal{I}_{\text{ind}}), \quad \text{where} \quad (9)$$

$$\mathcal{I}_{\text{ext}}(\kappa_{\text{TF}}a, \epsilon_I/\epsilon_{\text{II}}) = \int_0^{+\infty} d\lambda \frac{4(\epsilon_I/\epsilon_{\text{II}})\lambda e^{-2\lambda}}{\sqrt{\lambda^2 + (\kappa_{\text{TF}}a)^2} + (\epsilon_I/\epsilon_{\text{II}})\lambda} \quad (10)$$

$$\mathcal{I}_{\text{ind}}(\kappa_{\text{TF}}a, \epsilon_I/\epsilon_{\text{II}}) = \int_0^{+\infty} d\lambda \frac{2(\kappa_{\text{TF}}a)^2 \lambda e^{-2\lambda}}{\left((\epsilon_I/\epsilon_{\text{II}})\lambda + \sqrt{\lambda^2 + (\kappa_{\text{TF}}a)^2} \right)^2 \sqrt{\lambda^2 + (\kappa_{\text{TF}}a)^2}}. \quad (11)$$

\mathcal{I}_{ext} goes to unity for the insulating limit ($\kappa_{\text{TF}} = 0$, $\epsilon_I = \epsilon_{\text{II}}$) and vanishes for the ideal metal ($\kappa_{\text{TF}} \rightarrow \infty$). \mathcal{I}_{ind} vanishes in both limits. The detailed derivation can be found in the Appendix A. The total energy reads accordingly $U^{(1)} = U_{\text{ext}}^{(1)} + U_{\text{ind}}^{(1)}$, separating the two induced and external contributions $U_{\text{ext}}^{(1)} = -\frac{Q^2}{16\pi\epsilon_0\epsilon_I a} (1 - \mathcal{I}_{\text{ext}})$ and $U_{\text{ind}}^{(1)} = -\frac{Q^2}{16\pi\epsilon_0 a} \mathcal{I}_{\text{ind}}$. The integral expression \mathcal{I}_{ext} was first given in ref. 43 and 50, while we are not aware of \mathcal{I}_{ind} being discussed in the literature. In Fig. 2 we show the integrals and their influence on the total one-body

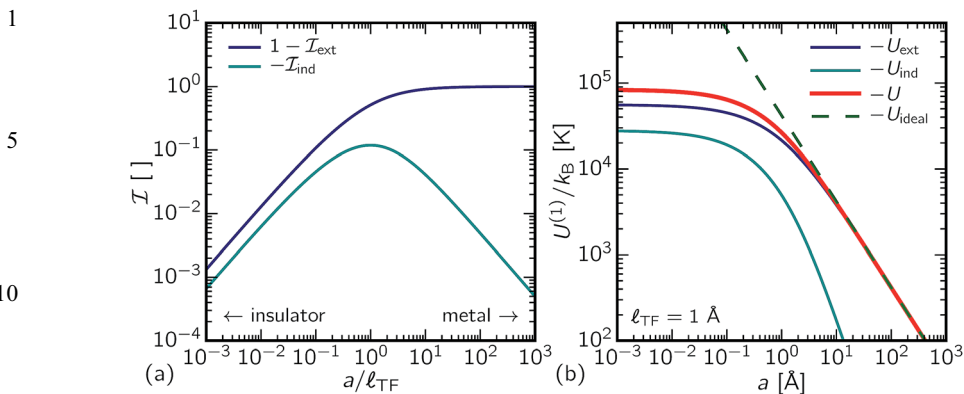


Fig. 2 (a) Dependence of integrals \mathcal{I} on the dimensionless distance to surface $a/l_{\text{TF}} = \kappa_{\text{TF}}a$; the TF metal behaves like a metal at long distances and like an insulator at short distances. The integrals represent the relative magnitude with regards to $U^{(1)}$ at the ideal metal limit $l_{\text{TF}} = 0$. \mathcal{I}_{ext} and \mathcal{I}_{ind} are associated with the external charge and the charge induced in the metal, respectively. Note the sign inversion for clarity. (b) The single-body electrostatic energy $U^{(1)} = U_{\text{ext}}^{(1)} + U_{\text{ind}}^{(1)}$ as a function of distance a for fixed $l_{\text{TF}} = 1 \text{ \AA}$. The finite screening length l_{TF} assures that $U^{(1)}$ has a finite value at the surface, unlike the divergence in the case of an ideal metal U_{ideal} . For all quantities shown, we impose no dielectric contrast ($\epsilon_{\text{I}} = \epsilon_{\text{II}} = 1$).

energy $U^{(1)}$. The energy is thus expressed in terms of a single-parameter integral with fast convergence due to the exponential decay of the integrands.

The reduction in energy of a charge close to the metal comes from the lowered electric field density, as the grounded surface only permits dipolar terms at long distances; the presence of the resulting electric field only in a half-space also explains why image charges contribute only half the energy when interacting with real charges. The one-body contribution $U^{(1)}(a)$ for TF metal thus interpolates between this value and the insulator limit.

At distances $a \gg l_{\text{TF}} = \kappa_{\text{TF}}^{-1}$, the TF potential energy approaches the ideal metal value $U_{\text{ext}}^{(1)}(\kappa_{\text{TF}} = \infty)$. But differences become apparent at shorter distances. Indeed the ideal metal energy diverges as a becomes small, due to the induced surface charge being localised laterally at distances comparable to a . But it is finite in the TF case, because the induced charge always has the extent of l_{TF} , thus providing a natural ultra-violet cut-off for the energy. Moreover, there is an additional energy term $U_{\text{ind}}^{(1)}$ associated with the induced TF charge in the metal. This term vanishes at the ideal metal limit, as the charge is confined to the surface and occupies no volume. It also vanishes at the insulator limit, where no charge can be induced. This induced charge energy contributes the most for intermediate distances $a \sim l_{\text{TF}}$.

From a practical point of view, *e.g.* for simulation purposes, we propose a more tractable expression for the interaction energy, in terms of rational functions. Such a rational function was among approximations for $U_{\text{ext}}^{(1)}$ proposed in ref. 44, which focused on the role of dielectric contrast. Here we fix $\epsilon_{\text{I}} = \epsilon_{\text{II}} = 1$ and approximate the integrals in eqn (10) and (11) to a higher degree of accuracy using a seven-parameter approximation of $U^{(1)}(a)$, reading

$$U^{(1)}(a) \simeq -\frac{Q^2}{16\pi\epsilon_0 a} \times \left[1 - \frac{13.8879(\kappa_{\text{TF}}a)^3 + 37.4625(\kappa_{\text{TF}}a)^2 + 18.6940(\kappa_{\text{TF}}a) + 1}{27.8648(\kappa_{\text{TF}}a)^4 + 73.0987(\kappa_{\text{TF}}a)^3 + 70.3460(\kappa_{\text{TF}}a)^2 + 20.6754(\kappa_{\text{TF}}a) + 1} \right] \quad (12)$$

with a maximal relative error of less than 10^{-5} . We give details of the fitting procedure in the Appendix A.

2.3 Two-body interaction: two interacting charges close to the TF surface

The surface also mediates additional interactions between charges, as the induced charge on the surface also acts on other external charges. We split the electrostatic potential energy due to the two-body interaction into three parts

$$U^{(2)}(r_1, r_2) = U_{\text{Coul}}^{(2)}(r_1, r_2) + U_{\text{ext}}^{(2)}(r_1, r_2) + U_{\text{ind}}^{(2)}(r_1, r_2), \quad (13)$$

where the individual parts represent the following interactions:

- $U_{\text{Coul}}^{(2)}$ = $Q_1 Q_2 / (4\pi\epsilon_0\epsilon_1 |r_1 - r_2|)$ is the direct Coulomb interaction between the two charges.

- $U_{\text{ext}}^{(2)}$ is the interaction of the charges with the charge induced in the TF boundary by the other charge. In the case of ideal metal this can be represented as half the Coulomb energy of each charge with the image charge of the other.

- $U_{\text{ind}}^{(2)}$ is the electrostatic energy of a charge distribution induced by one charge (and located in the vicinity of the interface inside the TF conductor) within the potential of the other.

As in eqn (8), the energy $U^{(2)}$ is a convolution of charge distribution with the potential. The terms $U_{\text{ext}}^{(2)}$ and $U_{\text{ind}}^{(2)}$ are of the form $(1/2) \int \psi^{(2)} \rho_{\text{ind}}^{(1)} + \psi^{(1)} \rho_{\text{ind}}^{(2)}$, comprising two contributions each. However, the two terms are equal, and we need to calculate only one of them, $\int \psi^{(2)} \rho_{\text{ind}}^{(1)}$. Altogether, the formal expressions for the two terms $U_{\text{ext}}^{(2)}$ and $U_{\text{ind}}^{(2)}$ are obtained as:

$$U_{\text{ext}}^{(2)}(\mathbf{r}_1, \mathbf{r}_2) = \frac{Q_1 Q_2}{4\pi\epsilon_0\epsilon_1} \int_0^\infty dK J_0 \left(K \left| \mathbf{r}_1^{(\parallel)} - \mathbf{r}_2^{(\parallel)} \right| \right) \frac{\epsilon_I K - \epsilon_{\text{II}} \sqrt{K^2 + \kappa_{\text{TF}}^2}}{\epsilon_I K + \epsilon_{\text{II}} \sqrt{K^2 + \kappa_{\text{TF}}^2}} e^{-K(z_1 + z_2)}, \quad (14)$$

where $r^{(\parallel)}$ denotes the projection of r parallel to the surface. And, using eqn (6) and (7), one has

$$U_{\text{ind}}^{(2)}(\mathbf{r}_1, \mathbf{r}_2) = \frac{1}{2} \int d\mathbf{r} \rho_{\text{ind}}(\mathbf{r}_2 | \mathbf{r}) \psi_{\text{II}}(\mathbf{r}_1 | \mathbf{r})$$

$$\psi_{\text{II}}(\mathbf{r}_1 | \mathbf{r}) = \frac{Q}{2\pi\epsilon_0} \int_0^\infty dK J_0 \left(K \left| \mathbf{r}^{(\parallel)} - \mathbf{r}_1^{(\parallel)} \right| \right) \frac{K e^{+z_1 \sqrt{K^2 + \kappa_{\text{TF}}^2}} e^{-Kz}}{\epsilon_I K + \epsilon_{\text{II}} \sqrt{K^2 + \kappa_{\text{TF}}^2}} \quad (15)$$

$$\rho_{\text{ind}}(r_2 | r) = -\frac{\epsilon_{\text{II}} \kappa_{\text{TF}}^2 Q}{2\pi} \int_0^\infty dK J_0 \left(K \left| r^{(\parallel)} - r_2^{(\parallel)} \right| \right) \frac{K e^{+z_2 \sqrt{K^2 + \kappa_{\text{TF}}^2}} e^{-Kz}}{\epsilon_I K + \epsilon_{\text{II}} \sqrt{K^2 + \kappa_{\text{TF}}^2}}$$

Formally, these terms can be presented once again as inverse Hankel transforms, but we could not succeed in inverting the integrals analytically. To proceed further, we explore the far-field behavior by formally expanding the integrals in powers of the TF length, l_{TF} , in the equivalent of a multipole expansion. This allows us to investigate the limit where l_{TF} is finite, but small, corresponding to a good, but not ideal, metal.

In order to simplify notations, we consider in the following a pair of charges Q_1 and Q_2 at respective positions $\mathbf{r}_1 = [x_1, y_1, z_1] = [0, 0, a]$ and $\mathbf{r}_2 = [x_2, y_2, z_2] = [d, 0, b]$; see Fig. 1 and 3a for sketches of this coordinate system used in deriving the two-charge energy terms.

“Image charge” contribution $U_{\text{ext}}^{(2)}$. The integral in eqn (14) closely resembles inverse transforms of functions of the type $K^M e^{-Kz}$, which can be resolved analytically. Thus, expanding the integrand in powers of l_{TF} , the resulting expansion in real space is a multipole series centred at the image charge location $\mathbf{r}'_1 = [0, 0, -a]$, with the distance between the image multipole and the charge being $r_{\text{im}} = \sqrt{d^2 + (a+z)^2}$. This yields immediately:

$$U_{\text{ext}}^{(2)}(\mathbf{r}_1, \mathbf{r}_2) = \frac{Q_1 Q_2}{8\pi\epsilon_0\epsilon_{\text{I}}} \left[-\frac{1}{r_{\text{im}}} + \frac{2\epsilon_{\text{I}}}{\epsilon_{\text{II}}\kappa_{\text{TF}}} \frac{\cos\psi}{r_{\text{im}}^2} - \frac{2\epsilon_{\text{I}}^2}{(\epsilon_{\text{II}}\kappa_{\text{TF}})^2} \frac{3\cos^2\psi - 1}{r_{\text{im}}^3} + \frac{3(2\epsilon_{\text{I}}^3 - \epsilon_{\text{I}}\epsilon_{\text{II}}^2)}{(\epsilon_{\text{II}}\kappa_{\text{TF}})^3} \frac{5\cos^3\psi - 3\cos\psi}{r_{\text{im}}^4} + \mathcal{O}\left(\frac{1}{\kappa_{\text{TF}}^4 r_{\text{im}}^5}\right) \right], \quad (16)$$

where $\cos\psi = (a+b)/r_{\text{im}}$; see Appendix B for details. The series is convergent for $r_{\text{im}} > l_{\text{TF}}$, which we find by comparing it with the expansion of the single body term $U_{\text{ext}}^{(1)}$. For practical implementation, a large margin $r_{\text{im}} > 2l_{\text{TF}}$ is suitable. Altogether, this means that the image charge is replaced by an image multipole series at long distances. We note that the multipole expansion constitutes an alternative derivation of the previously observed strong lateral dependence of the potential along the surface,^{19,43} as evidenced by the dipolar term scaling as $l_{\text{TF}}\epsilon_{\text{I}}/\epsilon_{\text{II}}$.

“Induced charge” contribution $U_{\text{ind}}^{(2)}$. The integrals in eqn (15) for the two-body potential energy of the induced charge distribution cannot be expanded *via* the same method as for $U_{\text{ext}}^{(2)}$, because $\chi_{\text{TF}} = \sqrt{K^2 + \kappa_{\text{TF}}^2}$ appears in the exponential in the integral expressions for the potential and induced charge, see eqn (15): the term $e^{\chi_{\text{TF}}z}$ has an essential singularity at $l_{\text{TF}} \rightarrow 0$ and as such does not allow for an expansion in l_{TF} .

However one may remark that physically, any perturbing charge is screened at the Thomas–Fermi length $l_{\text{TF}} = 1/\kappa_{\text{TF}}$, and similarly, the external potential will decay exponentially away from the surface over a length l_{TF} . The charge distribution can thus be approximated by projecting the charge along the z -axis onto a single plane, and placing this flat distribution at the surface. This approximation amounts to the assumption that the induced charge varies in a thin layer, and moreover in a slow and controlled fashion; it follows that it is valid at distances larger than TF length and its relative error scales as $\min(a,b)/l_{\text{TF}}$.

We approximate accordingly the induced charge as an infinitesimally thin layer $\rho_{\text{ind}}^{\text{app}}(z, R) = \sigma_{\text{ind}}(R)\delta(z)$.

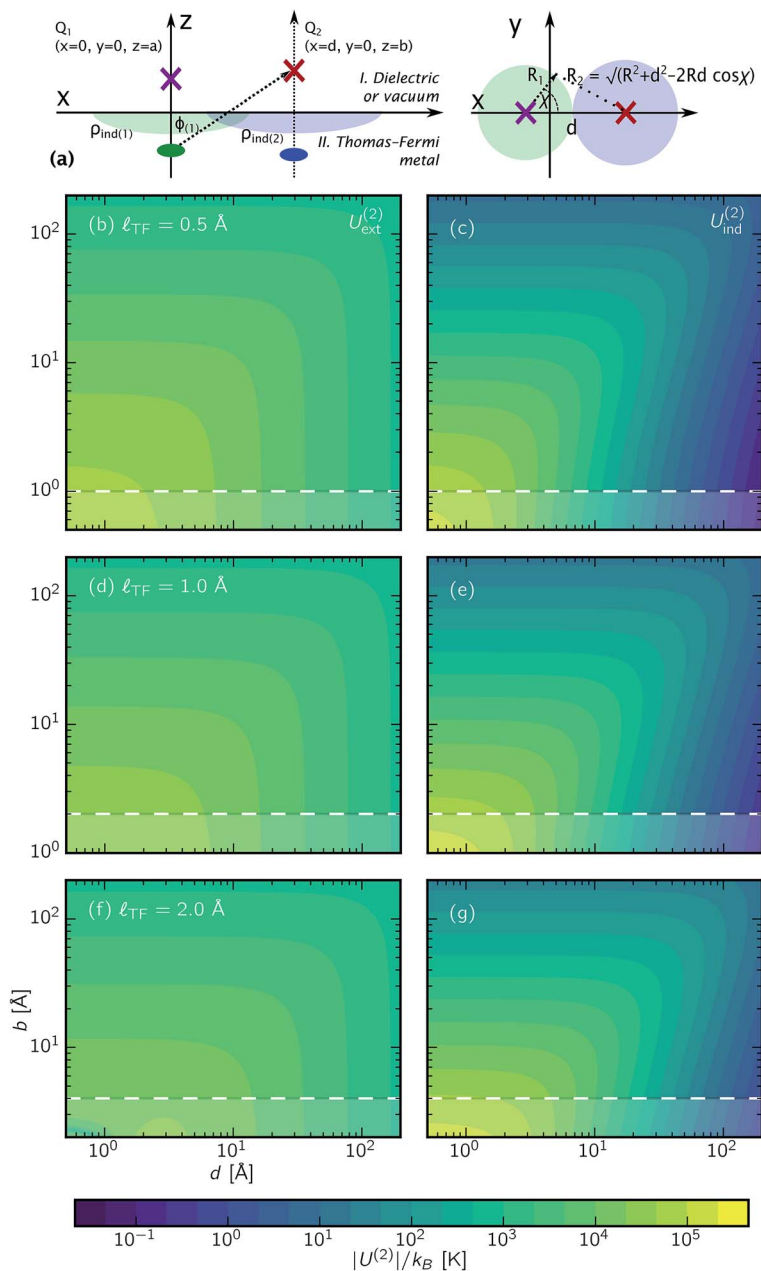


Fig. 3 (a) The coordinate system used in the main text to derive $U^{(2)}$. (b–g) Electrostatic two-body energy terms $U_{\text{ext}}^{(2)}$ (panels b, d and f) and $U_{\text{ind}}^{(2)}$ (panels c, e and g) due to the presence of TF metal, with examples given for $l_{\text{TF}} = 0.5 \text{ \AA}$ (b and c), $l_{\text{TF}} = 1 \text{ \AA}$ (d and e), and $l_{\text{TF}} = 2 \text{ \AA}$ (f and g). The charges are placed at $[0, 0, a = 1 \text{ \AA}]$ and $[d, 0, b]$, respectively. Only absolute values are plotted, and both terms are of the opposite sign to the direct Coulomb interaction, *i.e.* positive for $q_1 = -q_2 = e$. At long distances, U_{ext} converges to the image charge picture of the ideal metal limit, while U_{ind} decays as b^{-2} perpendicular, and as d^{-3} parallel to the surface with a shape that represents the lateral extent of the induced charge. The dashed white line corresponds to $b = 2l_{\text{TF}}$, giving an estimate of the convergence of the series for $U_{\text{ext}}^{(2)}$ and $U_{\text{ind}}^{(2)}$, as the series represents a long-range limit.

$$\begin{aligned}
 \sigma_{\text{ind}}(R) &= \beta \int_{-\infty}^0 dz \rho_{\text{ind}}(z, R) = -\beta \frac{\kappa_{\text{TF}}^2 Q}{2\pi} \int_{-\infty}^0 dz \int_0^{\infty} dK J_0(KR) \frac{\varepsilon_{\text{II}} K e^{+\sqrt{K^2 + \kappa_{\text{TF}}^2} z} e^{-Ka}}{\varepsilon_{\text{I}} K + \varepsilon_{\text{II}} \sqrt{K^2 + \kappa_{\text{TF}}^2}} \\
 &= -\beta \frac{Q}{2\pi} \int_0^{\infty} dK J_0(KR) \frac{\varepsilon_{\text{II}} \kappa_{\text{TF}}^2 K e^{-Ka}}{(\varepsilon_{\text{I}} K + \varepsilon_{\text{II}} \sqrt{K^2 + \kappa_{\text{TF}}^2}) \sqrt{K^2 + \kappa_{\text{TF}}^2}}.
 \end{aligned}
 \tag{17}$$

Because the projection is not an exact procedure, we introduce a scaling factor, β which we will fix *a posteriori* by examining some exact limiting cases.

This form can now be subject to the expansion in the Thomas-Fermi length l_{TF} resulting in

$$\begin{aligned}
 \sigma_{\text{ind}}(r_{\text{im}}, \psi) &= -\beta \frac{Q}{2\pi} \left[\frac{\cos \psi}{r_{\text{im}}^2} - \frac{\varepsilon_{\text{I}} (3 \cos^2 \psi - 1)}{\varepsilon_{\text{II}} \kappa_{\text{TF}} r_{\text{im}}^3} + \frac{3(\varepsilon_{\text{I}}^2 - \varepsilon_{\text{II}}^2) (5 \cos^3 \psi - 3 \cos \psi)}{\varepsilon_{\text{II}}^2 \kappa_{\text{TF}}^2 r_{\text{im}}^4} \right. \\
 &\quad \left. + \mathcal{O}\left(\frac{1}{\kappa_{\text{TF}}^3 r_{\text{im}}^5}\right) \right], \text{ for } r \text{ confined to the plane } (z = 0).
 \end{aligned}
 \tag{18}$$

Along the same lines, in the thin layer approximation the potential writes

$$\begin{aligned}
 \psi_{\text{II}}(a|R, z) &\simeq \kappa_{\text{TF}} \frac{Q}{2\pi \varepsilon_{\text{II}} \varepsilon_0 \kappa_{\text{TF}}^2} \left[\frac{\cos \psi}{r_{\text{im}}^2} - \frac{\varepsilon_{\text{I}} (3 \cos^2 \psi - 1)}{\varepsilon_{\text{II}} \kappa_{\text{TF}} r_{\text{im}}^3} \right. \\
 &\quad \left. + \frac{3(\varepsilon_{\text{I}}^2 - \varepsilon_{\text{II}}^2) (5 \cos^3 \psi - 3 \cos \psi)}{\varepsilon_{\text{II}}^2 \kappa_{\text{TF}}^2 r_{\text{im}}^4} + \mathcal{O}\left(\frac{1}{\kappa_{\text{TF}}^3 r_{\text{im}}^5}\right) \right]
 \end{aligned}
 \tag{19}$$

This term scales with the dielectric contrast $l_{\text{TF}} \varepsilon_{\text{I}} / \varepsilon_{\text{II}}$, paralleling eqn (16).

Combining these two contributions provides an expansion in powers of $1/\kappa_{\text{TF}}$. Focusing here on the lowest order term, proportional to $1/\kappa_{\text{TF}}$, the corresponding “dipolar” term of the convolution of σ_{ind} and ψ_{II} reads in the coordinate system introduced above:

$$\begin{aligned}
 U_{\text{ind}}^{(2)}(a, b, d) &\simeq -\frac{\beta Q_1 Q_2}{8\pi \varepsilon_{\text{II}} \varepsilon_0 \kappa_{\text{TF}}} \frac{1}{\pi} \int_0^{\infty} dR \\
 &\quad \times \int_0^{2\pi} d\chi \frac{Ra}{(a^2 + R^2)^{3/2}} \frac{b}{(b^2 + d^2 + R^2 - 2Rd \cos \chi)^{3/2}} + \mathcal{O}\left(\frac{1}{\kappa_{\text{TF}}^2}\right) \\
 &= -\frac{\beta Q_1 Q_2 ab}{8\pi \varepsilon_{\text{II}} \varepsilon_0 \kappa_{\text{TF}}} \frac{1}{\pi} \int_0^{\infty} dR \frac{4R \varepsilon \left(\frac{4dR}{b^2 + (d+R)^2} \right)}{(a^2 + R^2)^{3/2} (b^2 + (d-R)^2) (b^2 + (d+R)^2)^{1/2}} \\
 &\quad + \mathcal{O}\left(\frac{1}{\kappa_{\text{TF}}^2}\right)
 \end{aligned}
 \tag{20}$$

where ε is the complete elliptic integral. This integral is not expressible in a closed form, but converges quickly due to its d^{-5} asymptotics.

Interestingly, for the specific case of $d \rightarrow 0$ and $a = b$ (same axis), the expansion for $U_{\text{ind}}^{(2)}$ converges to a finite value which can be obtained readily as

$$U_{\text{ind}}^{(2)}(a, b = a, d = 0) = -\frac{\beta Q^2}{16\pi\epsilon_{\text{II}}\epsilon_0 a} \left[\frac{1}{\kappa_{\text{TF}} a} - \frac{2\epsilon_{\text{I}}}{\epsilon_{\text{II}}} \frac{1}{(\kappa_{\text{TF}} a)^2} + \mathcal{O}\left(\frac{1}{\kappa_{\text{TF}}^3}\right) \right]. \quad (21)$$

This corresponds to two coinciding charges and this should match the corresponding series for the self-energy term $U_{\text{ind}}^{(1)}$ in eqn (9), which is shown to behave as

$$U_{\text{ind}}^{(1)}(a) = -\frac{Q^2}{16\pi\epsilon_0 a} \left[\frac{1}{2\kappa_{\text{TF}} a} - \frac{\epsilon_{\text{I}}}{\epsilon_{\text{II}}} \frac{1}{(\kappa_{\text{TF}} a)^2} + \mathcal{O}\left(\frac{1}{\kappa_{\text{TF}}^3}\right) \right]. \quad (22)$$

So the comparison between the two expressions confirms the thin layer expansion as a valid approach, and allows the scaling factor β to be fixed to a value $\beta = \epsilon_{\text{II}}/2$.

Altogether, and to the lowest order in κ_{TF}^{-1} (“dipolar contribution”), we accordingly obtain the expression:

$$U_{\text{ind}}^{(2)}(a, b, d) \simeq -\frac{Q_1 Q_2}{16\pi\epsilon_0 \kappa_{\text{TF}}} \frac{1}{\pi} \int_0^\infty dR \frac{4Rab\epsilon \left(\frac{4dR}{b^2 + (d+R)^2} \right)}{(a^2 + R^2)^{3/2} (b^2 + (d-R)^2) (b^2 + (d+R)^2)^{1/2}} + \mathcal{O}\left(\frac{1}{\kappa_{\text{TF}}^2}\right). \quad (23)$$

This leading term decays as b^{-2} perpendicular, and as d^{-3} parallel to the surface (see Fig. 3); the subsequent corrections are of higher order in the charge distance. Better apparent from the expression (14), $U_{\text{TF}}(a, b, d)$ is a function of $a + b$ and d only. It can again be well approximated by rational functions of these variables, thus allowing for a more efficient evaluation in molecular simulations. This expression is provided in the Appendix B.

We finally mention that higher order terms in $1/\kappa_{\text{TF}}^2, \dots$ can be obtained by combining corresponding terms in eqn (18) and (19). We however leave these technical but straightforward calculations for future work.

Summary: total electrostatic interaction. The expression for the total electrostatic interaction potential, expressed formally in eqn (13), can be obtained as the sum of the coulombic interaction, $U_{\text{Coul}}^{(2)} = Q_1 Q_2 / (4\pi\epsilon_0 \epsilon_{\text{I}} |r_1 - r_2|)$, and two contributions resulting from image and induced charges, $U_{\text{ext}}^{(2)}$ and $U_{\text{ind}}^{(2)}$. Analytical expressions for these interaction energies can be obtained in the limit of small TF length, l_{TF} (or large κ_{TF}) in terms of a multipole-like expansion. The corresponding expressions are obtained in eqn (16) and (23). It is provided at the lowest (dipolar) order in $1/\kappa_{\text{TF}}$ for $U_{\text{ind}}^{(2)}$. Higher order terms can be obtained by going up in the expansion. They constitute practical expressions which can be used to calculate the many-body electrostatic energy of multiple charges in interaction, when located in the vicinity of a TF metal.

Altogether, the electrostatic interaction potential is plotted in Fig. 4 for various distances and TF lengths.

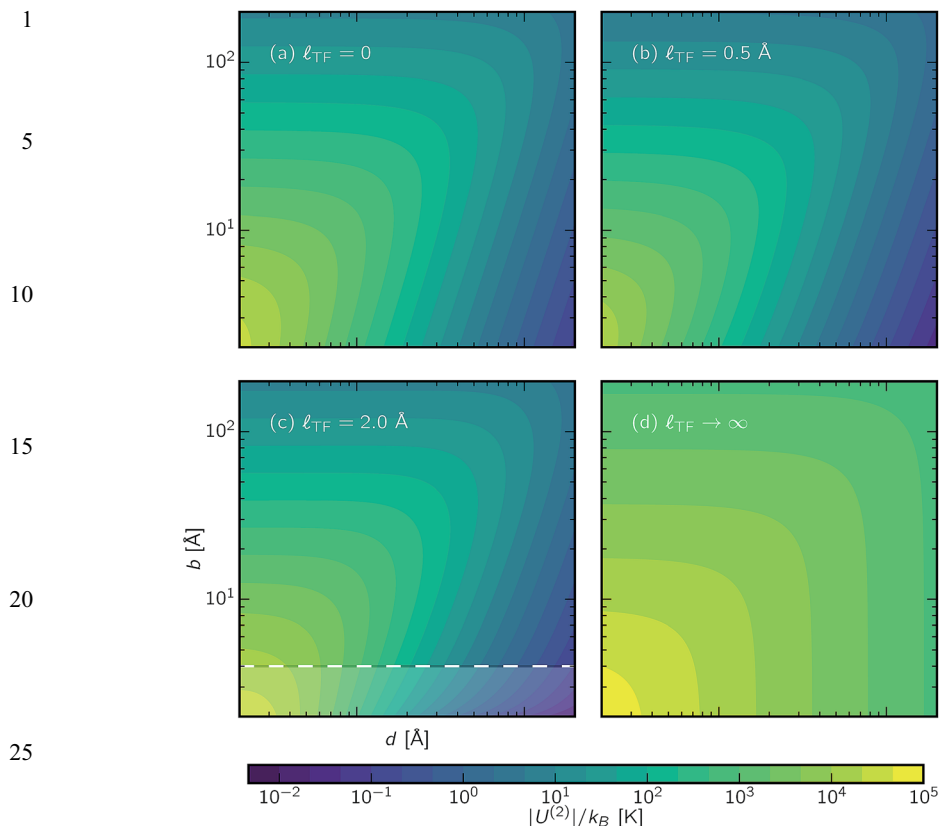


Fig. 4 The total electrostatic energy of two-charge configurations at $[0, 0, a = 1 \text{ \AA}]$ and $[d, 0, b]$ for $l_{\text{TF}} = 0$ (a), $l_{\text{TF}} = 0.5 \text{ \AA}$ (b), $l_{\text{TF}} = 2 \text{ \AA}$ (c), and $l_{\text{TF}} = \infty$ (d). The long-range dipolar character from the ideal metal case is preserved for small TF lengths, while the absolute values shift. This is representative of the perturbation approach we take. The dashed white line corresponds to $b = 2l_{\text{TF}}$, giving an estimate of convergence of the series.

3 The one dimensional ionic crystal and the role of electronic screening in interfacial energy

The previous calculations do show that the interaction of charges in the vicinity of a TF substrate can be formally complex and non-trivial. In this section, we use the previous framework on a simplified one dimensional crystal system. This allows us to gain many physical insights into the behavior of the TF screening and will provide explicit expressions for the electrostatic contribution to the crystal-substrate surface tension, as a function of the electronic structure of the walls.

We consider a one-dimensional electroneutral crystal of $N/2$ cations and $N/2$ anions with a TF boundary. The inter-ion lattice spacing is denoted as α and the crystal charge distribution reads

$$\rho_{\text{cr}}^{(N)}(z, R) = \sum_{n=0}^N (-1)^n \frac{Q\delta(z - (n\alpha + h))\delta(R)}{2\pi R}. \quad (24)$$

Here h is the shift of the first layer close to the wall; in the following we will mostly focus on the case where $h = \alpha/2$.

From a technical point of view, calculating energies of such long-range interacting crystals requires precise definition of the convergence of the sums involved.³⁰ One of the key observations is that boundary conditions need to be imposed even for an infinite system,³¹ resulting in surface energy terms for pairs of boundaries that cannot be disentangled to single boundary values. We analyze carefully the meaning of these surface terms, and use this framework to discuss surface energy and disjoining pressure.³²

3.1 Surface tension of an ionic crystal close to an insulating surface

The electrostatic energy of a crystal with finite thickness N , immersed in a dielectric with relative permittivity ϵ_1 can be calculated as

$$U(l_{TF} \rightarrow \infty; N) = \frac{Q^2}{4\pi\epsilon_1\epsilon_0\alpha} \sum_{n=1}^N \sum_{m=1}^{n-1} \frac{(-1)^{n-m}}{n-m} \\ = \frac{Q^2}{16\pi\epsilon_1\epsilon_0\alpha} \left[-4N \ln 2 + 2 - \frac{1}{N} + \mathcal{O}(N^{-3}) \right], \quad (25)$$

where we recall that α is the inter-ion lattice spacing. The sum is conditionally convergent, but we calculate the asymptotics by fixing the physical order of summation given by adding pairs of positive and negative charges. The potential energy per particle converges to the Madelung constant $\epsilon_{\text{Mad}} = -Q^2 \ln 2/4\pi\epsilon_1\epsilon_0\alpha$ for $N \rightarrow \infty$.

The surface energy for a crystal–insulating wall interface is then identified as

$$\gamma_{\text{ins}} = \gamma(l_{TF} \rightarrow \infty) = \frac{Q^2}{8\pi\epsilon_1\epsilon_0\alpha} \quad (26)$$

and for large film thickness, $D = N\alpha$, this value is approached with a long range $1/D$ correction as

$$W(l_{TF} \rightarrow \infty; D \gg \alpha) = \gamma_{\text{ins}} - \frac{Q^2}{16\pi\epsilon_1\epsilon_0 D} + \dots \quad (27)$$

Several remarks are in order. First, the finite thickness correction to the surface energy (corresponding to an insulator–crystal–insulator interface) is shown to vanish with the inverse thickness D^{-1} and is therefore of considerably long range, longer than van der Waals interactions which decay with D^{-2} . Furthermore the electrostatic nature of the interaction leads to typical surface energies in the order of $Q^2/16\pi\epsilon_1\epsilon_0\alpha^3$ (normalizing by an elementary area α^2). For $\alpha = 3 \text{ \AA}$, a typical inter-ion spacing in ionic liquids, this yields large values for the surface energy, of the order 2 J m^{-2} , comparable with the adhesion energy of two metals.³² This is also much higher than the typical surface energy of a free ionic liquid interface, which is of the order of 50 mJ m^{-2} .³³

3.2 Surface tension of an ionic crystal close to a perfect metal surface

We now consider the situation of an ionic crystal with finite thickness sandwiched between a perfect metal surface on one side and a dielectric semi-infinite medium on the other. The potential energy of each charge in the crystal gains an additional

term, expressed as an interaction with image charges, although with half the energy of interaction with a real charge.^{23,29}

The energy can be summed to yield

$$\begin{aligned}
 U(l_{\text{TF}} \rightarrow 0; N) &= \frac{Q^2}{4\pi\epsilon_1\epsilon_0\alpha} \left[\sum_{n=1}^N \sum_{m=1}^{n-1} \frac{(-1)^{n-m}}{n-m} + \frac{1}{2} \sum_{n=1}^N \sum_{m=1}^N \frac{(-1)^{n+m-1}}{n+m-1} \right] \\
 &= \frac{Q^2}{16\pi\epsilon_1\epsilon_0\alpha} \left[-4N \ln 2 + 1 - \frac{1}{4N} + \mathcal{O}(N^{-3}) \right].
 \end{aligned}
 \tag{28}$$

Subtracting the Madelung contribution, $N \times \epsilon_{\text{Mad}}$, one obtains the surface energy for a crystal–metal wall interface as

$$\gamma_{\text{metal}} = \gamma(l_{\text{TF}} \rightarrow 0, N \gg 1) = \frac{Q^2}{16\pi\epsilon_1\epsilon_0\alpha}
 \tag{29}$$

Again this value for the energy is reached asymptotically – in this metal–crystal–dielectric geometry – with a long range correction scaling like the inverse film thickness

$$W(l_{\text{TF}} \rightarrow 0, D) = \gamma_{\text{metal}} - \frac{Q^2}{64\pi\epsilon_1\epsilon_0 D} + \dots
 \tag{30}$$

(again with $D = N\alpha$ the film thickness).

3.3 Surface tension of an ionic crystal close to a TF surface

Beyond these limiting situations, we now consider the more complex case of ionic crystals at the interface with a TF wall.

The expression of the energy is a charge–potential convolution, of the same form as for the one-body energy, eqn (8). We will use the ideal metal limit as a reference for the energy, as it greatly simplifies the calculations. Following the same procedures as in the previous section, the Hankel transform of the resulting “excess” potential of the n th charge is

$$\begin{aligned}
 \delta\psi_{\text{I}}(n\alpha + h|z, K) &= \psi_{\text{I}}(z, K) - \psi_{\text{I}}^{\text{metal}}(z, K) = \frac{Q}{4\pi\epsilon_0\epsilon_1 K} \frac{2\epsilon_1 K}{\epsilon_{\text{II}}\chi_{\text{TF}} + \epsilon_1 K} e^{-K(n\alpha+h)} e^{-Kz} \\
 \delta\psi_{\text{II}}(n\alpha + h|z, K) &= \psi_{\text{II}}(z, K) - \psi_{\text{II}}^{\text{metal}}(z, K) = \frac{Q}{4\pi\epsilon_0\epsilon_1 K} \frac{2\epsilon_1 K}{\epsilon_{\text{II}}\chi_{\text{TF}} + \epsilon_1 K} e^{-K(n\alpha+h)} e^{+\chi_{\text{TF}}z}.
 \end{aligned}
 \tag{31}$$

Differently to the metal case, the bulk Madelung term cancels out and this allows us to calculate directly the surface energy, $\gamma(l_{\text{TF}}, N)$. A straightforward calculation shows that the latter can then be written as the sum of three terms:

$$\gamma(l_{\text{TF}}, N) = \gamma(l_{\text{TF}} = 0, N) + \gamma_{\text{ext}}(l_{\text{TF}}, N) + \gamma_{\text{ind}}(l_{\text{TF}}, N).
 \tag{32}$$

The “external charge” contribution $\gamma_{\text{ext}}(l_{\text{TF}}, N)$ involves a double sum evaluating N contributions to the potential at N point charge positions. This yields a geometric sum, which can be brought under the integral to give

$$\begin{aligned}
 \gamma_{\text{ext}}(l_{\text{TF}}, N) &= \frac{Q^2}{8\pi\epsilon_0\epsilon_{\text{I}}} \int_0^{+\infty} dK \frac{2\epsilon_{\text{I}}K}{\epsilon_{\text{II}}\chi_{\text{TF}} + \epsilon_{\text{I}}K} e^{-2Kh} \sum_{n=0}^{N-1} \sum_{m=0}^{N-1} (-e^{-Ka})^{n+m} \\
 &= \frac{Q^2}{16\pi\epsilon_0\epsilon_{\text{I}}a} \int_0^{+\infty} d\lambda \frac{4(\epsilon_{\text{I}}/\epsilon_{\text{II}})\lambda}{(\epsilon_{\text{I}}/\epsilon_{\text{II}})\lambda + \sqrt{\lambda^2 + (\kappa_{\text{TF}}a)^2}} \frac{e^{-2\lambda(h/a)}(1 + (-1)^N e^{-N\lambda})^2}{(1 + e^{-\lambda})^2}.
 \end{aligned}
 \tag{33}$$

On the other hand, the energy shift due to the induced charge can be written as

$$\begin{aligned}
 \gamma_{\text{ind}}(l_{\text{TF}}, N) &= -\pi\epsilon_0\epsilon_{\text{II}}\kappa_{\text{TF}}^2 \int_{-\infty}^0 dz \int_0^{+\infty} dK \left[\sum_{n=0}^N \delta\psi_{\text{II}}(n\alpha + h|z, K) \right]^2 K \\
 &= -\frac{Q^2}{16\pi\epsilon_0a} \int_0^{+\infty} d\lambda \frac{2\lambda(\kappa_{\text{TF}}a)^2}{\sqrt{\lambda^2 + (\kappa_{\text{TF}}a)^2} \left[\frac{\epsilon_{\text{I}}}{\epsilon_{\text{II}}}\lambda + \sqrt{\lambda^2 + (\kappa_{\text{TF}}a)^2} \right]^2} \frac{e^{-2\lambda(h/a)}(1 + (-1)^N e^{-N\lambda})^2}{(1 + e^{-\lambda})^2}.
 \end{aligned}
 \tag{34}$$

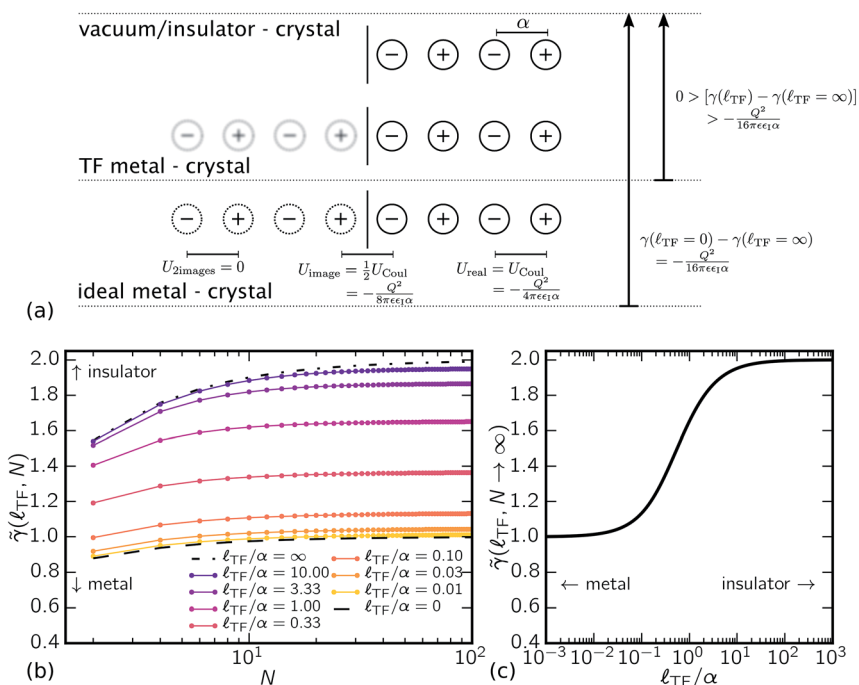


Fig. 5 The surface energy of a one-dimensional crystal close to the TF interface, as a function of its thickness N . (a) Schematic representation of the one-dimensional crystal and its limits. A crystal close to a metallic interface has a substantially lower energy than that close to an insulator, and TF theory interpolates between the two. (b) The surface energy γ as a function of crystal thickness N , for various TF lengths l_{TF} . The surface energy is adimensionalized by $Q^2/(16\pi\epsilon_0\epsilon_{\text{I}}\alpha)$. The dashed and dash-dotted lines show the ideal metal limit ($l_{\text{TF}} = 0$), and the insulator limit ($l_{\text{TF}} \rightarrow \infty$), respectively. (c) Dependence of the surface energy ($N = \infty$) versus the TF length.

1 where we recast the integral into a dimensionless form.

The surface tension $\gamma^{\text{TF}}(l_{\text{TF}})$ is obtained as the limit of this surface energy when $N = \infty$ and it takes the expression:

$$5 \quad \gamma^{\text{TF}}(l_{\text{TF}}) = \frac{Q^2}{16\pi\epsilon_1\epsilon_0\alpha} \mathcal{F}(\alpha/l_{\text{TF}}) \quad (35)$$

where $\mathcal{F}(\alpha/l_{\text{TF}}) = [1 + \mathcal{G}_{\text{ext}}(l_{\text{TF}}, \infty) - \mathcal{G}_{\text{ind}}(l_{\text{TF}}, \infty)]$ and \mathcal{G}_{ext} and \mathcal{G}_{ind} are the integrals in eqn (33) and (34), respectively, taken here in their $N = \infty$ limit.

10 We plot in Fig. 5b the dependence of the surface energy as a function of number of layers N for various TF lengths l_{TF} . In Fig. 5c, we then plot the dependence of $\gamma^{\text{TF}}(l_{\text{TF}})$ as a function of the TF length l_{TF} . This plot highlights that the TF interpolates smoothly between the insulating and ideal metal cases, as the TF length is varied between infinity and zero.

15 It is also interesting to extract the dependence of the electrostatic energy as a function of the number of layers N , *i.e.* the crystal thickness $D = N\alpha$. Such an expansion can be derived from the evaluation of a dipolar Ewald sum equivalent to eqn (28), yielding

$$20 \quad U(l_{\text{TF}}; D) = N \times \epsilon_{\text{Mad}} + W(D) \quad (36)$$

where the interfacial energy $W(D)$ of the TF metal–crystal–dielectric sandwich now writes

$$25 \quad W(D) = \gamma^{\text{TF}}(l_{\text{TF}}) - \frac{Q^2}{256\pi\epsilon_1\epsilon_0 D} - \frac{7Q^2 l_{\text{TF}}}{128\pi\epsilon_1\epsilon_0 D^2} + \mathcal{O}(D^{-3}), \quad (37)$$

30 As for the perfect metal and insulating cases, the first correction to the surface tension scales as a long-range $1/D$ term. But an interesting remark is that the thick film expansion for the crystal–TF metal interface reveals also the emergence of a term proportional to D^{-2} which is absent in both ideal metal and pure insulator cases. This term is akin to an attractive van der Waals potential, both in structure and in origin, as it follows from the interaction of charges with their image dipoles. It can be written in terms of a Hamaker constant for the TF metal–crystal–dielectric system, and takes the expression:

$$35 \quad A_{\text{TF-C-D}} = \frac{21l_{\text{TF}}Q^2}{32\epsilon_0\epsilon_1\alpha_{\parallel}^2}, \quad (38)$$

40 where TF–C–D stands for the TF metal–crystal–dielectric sandwich; we assumed that the lateral surface area corresponding to the one-dimensional crystal is α_{\parallel}^2 , the lateral size of the elementary cell. This yields $A_{\text{TF}} \approx 5 \times 10^{-18}$ J for typical values $\alpha_{\parallel} = 2$ Å and $l_{\text{TF}} = 1$ Å. So not only is the TF Hamaker contribution long-ranged, but it is of unusually high magnitude with this interfacial configuration.

3.4 Comparison to the direct numerical summation

50 As a final check for the previous approach, we compare in this section the exact result for the metal–crystal surface tension, in eqn (35), to the direct numerical summation of one body and two body interactions on a 1D crystalline structure, which are calculated using the TF formalism above. As described above, we

consider accordingly a one-dimensional electroneutral crystal of $N/2$ cations and $N/2$ anions (with position z_n , $n = 1, \dots, N$) at the interface with a TF metal wall.

The total energy is calculated *via* the direct summation of one-body and two-body interactions between ions.

$$U(N) = \sum_i U^{(1)}(z_i) + \frac{1}{2} \sum_{i \neq j} U^{(2)}(z_i, z_j) \quad (39)$$

where the expressions for $U^{(1)}$ and $U^{(2)}$ are given previously. Note that previously, we limited ourselves to a first order (in $1/\kappa_{\text{TF}}$) expression for $U^{(2)}$. This implies that, in order to be consistent, we only keep terms up to the dipolar order (linear in κ_{TF}^{-1}) in both expressions of $U_{\text{ext}}^{(2)}$ and $U_{\text{ind}}^{(2)}$ in eqn (16)–(23). The surface tension is deduced from the expression

$$\gamma^{\text{TF}} = \lim_{N \rightarrow \infty} [U(N) - N \times \varepsilon_{\text{Mad}}] \quad (40)$$

and in Fig. 6, we compare the exact result in eqn (35) to the direct numerical summation using the one body and two body interactions calculated over the ion structure. Note that the surface tension is made dimensionless according to $\gamma^{\text{TF}} = \frac{Q^2}{16\pi\varepsilon_0\alpha} \times \tilde{\gamma}^{\text{TF}}$. As expected, both results are shown to match for $\kappa_{\text{TF}}\alpha \gg 1$. Typically a 10% agreement is found for $\kappa_{\text{TF}}\alpha > 1.3$. This comparison therefore validates the previous framework developed for the calculation of TF interactions.

We conclude with two remarks. First, the agreement can be in principle improved by expanding the two-body interaction term further in powers of κ_{TF}^{-1} . We leave this development for future work. Second the results can be easily extended to higher dimensions. We have used the previous framework with approximated forms for the one-body and two body interactions to

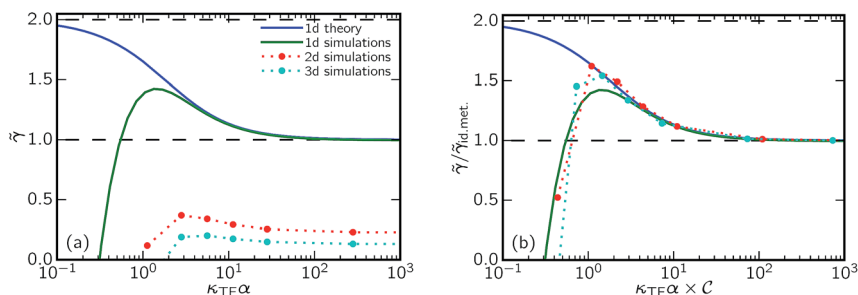


Fig. 6 Comparison of the 1D metal–crystal surface tension, from eqn (35) (green line), versus the direct summation of one body and two body interactions, from eqn (40) (blue line). As discussed in the text, the latter are calculated to first, dipolar, order in κ_{TF}^{-1} . A 10% agreement is found for $\kappa_{\text{TF}}\alpha > 1.3$. The surface tension is made dimensionless as $\tilde{\gamma}^{\text{TF}} = \gamma^{\text{TF}} / [Q^2/16\pi\varepsilon_0\alpha]$. The horizontal dashed lines are the 1D limits for insulating walls ($\tilde{\gamma}_{\text{ins}} = 2$, top) and perfect metals ($\tilde{\gamma}_{\text{id.met.}} = 1$, bottom). Two- and three-dimensional crystals (dotted lines) can be rescaled to closely follow the 1D energy function \mathcal{F} , as shown in (b). The rescaling parameters are $\tilde{\gamma}_{\text{ins}} = 2\tilde{\gamma}_{\text{id.met.}} \approx 0.46$, $C \approx 0.39$ for 2D square lattice, and $\tilde{\gamma}_{\text{ins}} = 2\tilde{\gamma}_{\text{id.met.}} \approx 0.26$, $C \approx 0.26$ for 3D cubic lattice.

1 calculate the energy in 2D and 3D semi-infinite system, from which we extract
the surface energy according to eqn (40). In Fig. 6, we show the numerical
estimate of the surface tension in 2D and 3D as a function of the TF screening
5 parameter, κ_{TF} . According to the theoretical framework (and in line with the 1D
results), we expect that the results are valid for sufficiently large TF screening
parameter, $\kappa_{\text{TF}}\alpha \gg 1$ with α the lattice spacing. Independently, the calculations
can also be performed for an insulating substrate, *i.e.* $\kappa_{\text{TF}} = 0$. An interesting
10 result is that whatever the dimension, we find that the surface tensions for the
perfect metal and insulating cases obey $\tilde{\gamma}_{\text{ins}} = 2\tilde{\gamma}_{\text{id.met}}$. Here $\tilde{\gamma}_{\text{ins}} = 2\tilde{\gamma}_{\text{id.met}} \approx$
 0.46 , for the 2D square lattice, and $\tilde{\gamma}_{\text{ins}} = 2\tilde{\gamma}_{\text{id.met}} \approx 0.26$, for the 3D cubic
lattice. This result calls for further analytical investigations. Finally, another
interesting result highlighted in Fig. 6b is that the surface tensions for the 2D
15 and 3D cases follow the same general scaling form *versus* κ_{TF} as the 1D case, up
to a simple rescaling: $\mathcal{F}_{2\text{D},3\text{D}}(\kappa_{\text{TF}}\alpha) \approx \mathcal{F}_{1\text{D}}(\mathcal{C}_{2\text{D},3\text{D}} \times \kappa_{\text{TF}}\alpha)$, with $\mathcal{F}_{1\text{D}}$ given in eqn
(35) and the rescaling constants provided in Fig. 6. This result highlights the
fact that although simplified, the 1D geometry captures the physics involved in
more complex interaction behavior with larger dimensions. We leave more
20 detailed calculations of surface tensions for a more exhaustive study involving
finite-temperature calculations using molecular simulations.

4 Towards the wetting properties of ionic liquids and crystals on metals

25 In this section we build on the previous results to discuss physically the relative
wetting of ionic liquids *versus* ionic crystals on metallic substrates.

This is motivated by our recent experimental results,¹¹ which point to the
capillary freezing of ionic liquids in confinement. These experiments highlight
30 the impact of the metallicity of the confining substrate to facilitate solidification
in a confined geometry. Capillary freezing can be interpreted in terms of the shift
of the freezing transition induced by surface wetting: while the stable phase in the
bulk is the ionic liquid, surface terms may become predominant in confinement,
favoring the thermodynamically less favored phase, which here is the crystal. This
35 mechanism is summarized by the so-called Gibbs–Thomson relationship
accounting for freezing in confinement.¹¹

At the core of this experimental result, the key question is to understand the
relative wettability of the crystal phase of the ionic system *versus* its liquid phase.
Our results above provide some key information on the wetting behavior of the
40 crystal phase. However, calculating analytically the surface tension for the ionic
liquid at a metal surface remains a tremendous task. Still, the high correlation
existing in an ionic liquid would suggest that the interfacial energy should behave
in quite a similar way to that of the crystal.

In the following, we discuss a simple framework allowing us to predict the
45 scaling behavior for the surface wettability of ionic systems on a metal, by taking
inspiration from the previous results for the crystal.

4.1 Approximated scaling of surface energies of crystals and liquids

50 Our approach is based on the following observation for the energetics of the ionic
crystal: the transition between metal and insulator follows a remarkably similar

function for the single-body potential energy $U^{(1)}$ in eqn (9)–(11) and for the surface tension γ^{TF} of the 1D crystal in eqn (33) and (34). This result is not coincidental and can actually be read directly from the detailed definitions of these terms, in terms of their integral expressions which are remarkably similar – compare eqn (9)–(11) with eqn (33) and (34). Graphically, this is also evidenced by comparing Fig. 5c and 2a.

Combined with the re-scaling of 2D and 3D surface tensions to match them with the 1D crystal function in Fig. 6, this allows us to propose that the surface tension follows a general scaling form

$$\gamma_{\text{cr}}^{\text{TF}} - \gamma_{\text{cr}}^{\text{ins}} \approx \rho_{\text{cr}} \times \alpha \times U^{(1)}(l_{\text{TF}}, \alpha) \quad (41)$$

where $\gamma_{\text{cr}}^{\text{ins}}$ is the surface tension with the insulating wall, here considered as reference.

But beyond the mathematical coincidence, the physical meaning behind this simple approximated form is simple and transparent. It shows that the dominant part of the surface energy originates in the interaction of ions in the vicinity of the walls with their image charges – *via* $U^{(1)}$. These contributing charges are typically at a molecular distance α from the surface – as evidenced by eqn (41) – their interaction energy scales accordingly with their number $N_{\text{cr}} \sim \alpha \times \rho_{\text{cr}}$. The contribution of the layers beyond a molecular distance α is screened out due to the compensation of near charges due to electroneutrality. This simple result is quite remarkable in the sense that it captures the main behavior for a complex interface between a dense and strongly interacting phase and an imperfect metal.

We note that this approximation of the surface tension curves corresponds to a situation where all of the individual surface-mediated interactions decay in a common way with the strength of the screening. The pre-factor is then given mainly by the geometry of the charge configurations. The independence of the geometry of the transition from an insulator to a metal thus requires that the two-body interactions are either sufficiently isotropic or weak (compared to one-body terms). Equivalently, we expect this assumption to fail if the effect of the surface leads to a great anisotropy. As the strongest lateral interaction scales as $l_{\text{TF}}\epsilon_{\text{I}}/(\epsilon_{\text{II}}d^3)$, see eqn (16), this approximation is expected to break down in the situations of a large dielectric contrast $\epsilon_{\text{I}} \gg \epsilon_{\text{II}}$. This regime was examined in detail and shown to exhibit a range of unique behaviour in ref. 19 and 43.

Coming back to the wetting of the ionic system, one may then remark that being physically simple, the previous scaling argument can be extended to any configuration of charges, and notably for the surface energy of an ionic liquid phase close to a TF metal. Following the above qualitative argument, the surface energy in excess to the insulating case is expected to scale as

$$\gamma_{\text{liq}}^{\text{TF}} - \gamma_{\text{liq}}^{\text{ins}} \approx \rho_{\text{liq}} \times a \times U^{(1)}(l_{\text{TF}}, a). \quad (42)$$

where the density of the liquid ρ_{liq} replaces the crystal one. The physical meaning is the same as above: it states that the main behavior for the liquid–wall interaction stems from the interaction of ions in the liquid phase located in

1 a molecular volume of extension a close to the metal. As for the crystal phase, the
size of this volume is fixed by electroneutrality which leads to a cut-off of inter-
action beyond a molecular length a . Being a dense phase, the characteristic length
5 a is expected to be typically of the order of the molecular size of the ions. This
range is thus expected of the same order of magnitude as the crystal lattice
spacing $a \approx \alpha$. We can take the same value of $a \approx \alpha$ for both the liquid and crystal
(chosen here as the crystal lattice spacing in the crystal), since this choice does not
make a strong difference in the functional dependence of $\mathcal{U}^{(1)}$.

10 We emphasize that this expression is only approximate, but that this approx-
imation is expected to capture the main contributions for the surface energy, as
validated by the exact benchmarking calculations above for the crystal–metal
interface. We discuss below the implications of this result for the wetting prop-
erties of ionic systems on metallic surfaces.

15 **4.2 Discussion: relative wetting of ionic crystal and liquid phases on a metal**

The previous results suggest that an increased ‘metallicity’ of the metals does
reduce the interfacial energy, thus stabilizing dense ionic phases close to metallic
substrates. Furthermore the decrease in surface energy is expected to be higher
20 for the denser crystal phase than its disordered liquid counterpart ($\rho_{\text{cr}} > \rho_{\text{liq}}$). This
is highlighted by the comparison of eqn (41) and (42). The difference becomes
more significant with decreasing l_{TF} (increasing κ_{TF}), and the metallicity of the
substrate thus promotes the wetting of the metal by the crystal phase, hereby
yielding ionic liquid crystallisation in confinement. This prediction, while based
25 on a simple mechanism, is in agreement with the experimental results obtained
in ref. 11.

Going beyond would require full molecular simulations to be performed to
study the relative wetting of the two phases at a metal surface. This will be the
objective of a future and dedicated study using molecular simulations, based on
30 the TF interaction potentials derived above.

5 Conclusions and perspectives

35 Our results above constitute a thorough exploration of the energetics of
charged systems in contact with Thomas–Fermi metal substrates, building on
and extending the previous theoretical work. We focus not only on the potential
outside of the metal, but also on the energy associated with inducing the TF
charge distribution in the surface, which is absent from previous work on the
40 subject. We put emphasis on deriving the results in a form applicable in
molecular simulations. Our analysis of the two-body potential energy reveals
a hitherto unknown structure involving a multipole expansion, which provides
a physical intuition into the far-field structure of the potential. It complements
the previous models of the “image charge on a line” approach of ref. 50 and the
45 “sandwich” of a dielectric and a perfect metal layer,⁴³ while being simpler than
the former and more precise than the latter. The expansions open the way for
simulations of conducting surfaces that are cheaper than full DFT, yet more
versatile than simulation methods for ideal (insulating or perfect metal)
50 surfaces. While the presented results involve a single conducting and a single

1 metallic wall, the approximation procedures can be repeated for combinations
of conducting walls.

2 Then, we have made use of this framework to obtain approximate expressions
3 for the surface tension of ionic systems at a metal wall, both for their ordered
4 crystal phase, and their disordered liquid phase. This is based on an analysis of
5 the crystal–metal interface, for which analytical results can be obtained with
simple physical interpretation in terms of the interaction of ions with their image
charges at the interface. It suggests an extension to the interface between an ionic
liquid and the metal substrates. This study indicates that wall metallicity favors
10 the denser crystal phase, and this effect is promoted for better metals. Altogether
it is particularly interesting, and quite counter-intuitive, that the electronic
screening in the metal, as characterized by a molecular length l_{TF} , profoundly
affects the interfacial energy of a crystal.

15 These results call for further extension in various directions. First, as discussed
above, it is now required to assess this scenario using molecular simulations and
perform a complete study of the wetting of ionic systems at (imperfect) metals.
Beyond the relative wettability of the ionic crystal *versus* the ionic liquid, it would
be also interesting to consider the wetting of thick films of crystal on the metal
20 surface. As we have shown above, asymptotic expansions for the 1D crystal case
show that the thickness dependence of the interfacial energy of a metal–crystal–
dielectric sandwich behaves as

$$W(D) = \gamma^{\text{TF}}(l_{\text{TF}}) - \frac{A_{\text{el}}}{D} - \frac{A_{\text{TF-C-D}}}{D^2} + \dots \quad (43)$$

25 where A_{el} is a pure electrostatic constant, and $A_{\text{TF-C-D}}$ is a Hamaker-like constant
for the TF metal–crystal–dielectric sandwich, whose expression is given in eqn
(38) and depends linearly on the TF length l_{TF} (for small l_{TF}). This suggests long-
range electrostatic interactions within the films (here calculated in the metal–
crystal–dielectric geometry). However this behavior needs to be confirmed in
30 molecular simulations in a more pertinent configuration, involving a metal–
crystal–liquid sandwich, at finite temperature. To some extent, these results echo
long-range electrostatic interactions observed recently,¹⁰ a relation between
confinement and correlations yet to be assessed in detail.

35 Taking a broader perspective, we conclude with several remarks about several
experimental situations, involving solid–electrolyte interfaces, where the elec-
tronic properties of the confining system could play a role.^{15,35–38} Recent experi-
mental work highlighted much faster hydrodynamic water flows inside single
(semi-metallic) carbon nanotubes as compared to (insulating) boron-nitride
40 nanotubes.³⁵ This puzzling result points to the fact that the understanding of
the interfacial interactions of charged and polarized molecules as well as the ionic
adsorption at metallic *versus* insulating surfaces is of primary interest in the
context of nanofluidic transport.^{40,41} Altogether, whether electronic properties
may affect hydrodynamics remains an open question. Using the simplified TF
45 model for the electronic properties of the substrates, as developed in the present
framework, could provide the first hints into the microscopic phenomena at
stake.

50 We finally quote that the present results could be generalized to alternative
experimental situations. Indeed our results apply for any boundary between
Laplace and Helmholtz equations. Accordingly the Thomas–Fermi framework

discussed here also applies to electrolyte solutions with a differential salt concentration, as evidenced by electrode adsorption being one of the original contexts for this model.^{45,47} From a practical point of view, the TF model is formally equivalent to the Debye–Hückel model for weak electrolytes,³⁴ where a metallic wall is equivalent to a salt solution with a corresponding Debye screening parameter, now defined in terms of the salt concentration. The subtle impact of the TF screening on the charge interactions obtained here suggests that similar effects could occur whenever charges are in the presence of an electrolyte with a differential salt concentration. In particular, this raises a number of questions about ionic interactions in the presence of salinity gradients, which would be interesting to explore more specifically. Moreover, the theory can be extended to the interface between a Debye–Hückel electrolyte and a Thomas–Fermi metal.⁵¹ Such situations are in particular relevant to a number of recent experimental observations associated with (diffusio-)osmosis and osmotic power generation under salinity gradients.⁴²

A Appendix: one-body potential energy

In this appendix, we detail how the definition of one-body potential energy in eqn (8) leads to eqn (9).

A.1 External charge potential energy

We begin with the energy of the external charge

$$U_{\text{ext}}^{(1)}(a) = \pi \int_{-\infty}^{+\infty} dz \int_0^{+\infty} dK K \left(\frac{Q\delta(z-a)}{2\pi} \right) \left(\frac{Q}{4\pi\epsilon_0\epsilon_I K} e^{-Kz} \left[e^{+Ka} - \frac{\epsilon_{II}\chi_{TF} - \epsilon_I K}{\epsilon_{II}\chi_{TF} + \epsilon_I K} e^{-Ka} \right] \right) \quad (44)$$

$$U_{\text{ext}}^{(1)}(a) = \frac{Q^2}{8\pi\epsilon_0\epsilon_I} \int_0^{+\infty} dK \left[1 - \frac{\epsilon_{II}\sqrt{K^2 + \kappa_{TF}^2} - \epsilon_I K}{\epsilon_{II}\sqrt{K^2 + \kappa_{TF}^2} + \epsilon_I K} e^{-2Ka} \right] \quad (45)$$

The first term is the divergent part of the self energy which is independent of the surroundings of the charge and can be therefore neglected. We recast the remaining part in terms of a dimensionless variable $\lambda = Ka$

$$U_{\text{ext}}^{(1)}(a) = -\frac{Q^2}{16\pi\epsilon_0\epsilon_I a} \int_0^{+\infty} d\lambda \frac{\sqrt{\lambda^2 + (\kappa_{TF}a)^2} - (\epsilon_I/\epsilon_{II})\lambda}{\sqrt{\lambda^2 + (\kappa_{TF}a)^2} + (\epsilon_I/\epsilon_{II})\lambda} 2e^{-2\lambda} \quad (46)$$

$$U_{\text{ext}}^{(1)}(a) = -\frac{Q^2}{16\pi\epsilon_0\epsilon_I a} + \frac{Q^2}{16\pi\epsilon_0\epsilon_I a} \int_0^{+\infty} d\lambda \frac{2(\epsilon_I/\epsilon_{II})\lambda}{\sqrt{\lambda^2 + (\kappa_{TF}a)^2} + (\epsilon_I/\epsilon_{II})\lambda} 2e^{-2\lambda} \quad (47)$$

$$U_{\text{ext}}^{(1)}(a) = -\frac{Q^2}{16\pi\epsilon_0\epsilon_I a} [1 + \mathcal{I}_{\text{ext}}], \quad (48)$$

which we separated into the ideal metal part and its correction. The limits yield correct results for the well-known cases of ideal dielectric and ideal metal

$$U_{\text{ext}}^{(1)}(a; \kappa_{\text{TF}} = 0) = -\frac{Q^2}{16\pi\epsilon_0\epsilon_1 a} \frac{\epsilon_{\text{II}} - \epsilon_1}{\epsilon_{\text{II}} + \epsilon_1} \int_0^{+\infty} d\lambda 2e^{-2\lambda} = -\frac{Q^2}{16\pi\epsilon_0\epsilon_1 a} \frac{\epsilon_{\text{II}} - \epsilon_1}{\epsilon_{\text{II}} + \epsilon_1} \quad (49)$$

$$U_{\text{ext}}^{(1)}(a; l_{\text{TF}} = 0) = -\frac{Q^2}{16\pi\epsilon_0\epsilon_1 a} \int_0^{+\infty} d\lambda 2e^{-2\lambda} = -\frac{Q^2}{16\pi\epsilon_0\epsilon_1 a}. \quad (50)$$

The integral (46) can be easily evaluated numerically due to its exponential decay and can be either tabulated for a convenient set of surface distances a , or approximated by a rational function. We give the expansion of the pre-factor of the exponential in l_{TF}/a

$$U_{\text{ext}}^{(1)}(a) = -\frac{Q^2}{16\pi\epsilon_0\epsilon_1 a} \int_0^{+\infty} d\lambda \frac{\sqrt{\lambda^2 + (\kappa_{\text{TF}}a)^2} - (\epsilon_1/\epsilon_{\text{II}})\lambda}{\sqrt{\lambda^2 + (\kappa_{\text{TF}}a)^2} + (\epsilon_1/\epsilon_{\text{II}})\lambda} 2e^{-2\lambda} \quad (51)$$

$$U_{\text{ext}}^{(1)}(a) = -\frac{Q^2}{16\pi\epsilon_0\epsilon_1 a} \int_0^{+\infty} d\lambda 2e^{-2\lambda} \left[1 - \frac{2\epsilon_1}{\epsilon_{\text{II}}} \frac{l_{\text{TF}}}{a} \lambda + \frac{2\epsilon_1^2}{\epsilon_{\text{II}}^2} \frac{l_{\text{TF}}^2}{a^2} \lambda^2 - \frac{(2\epsilon_1^3 - \epsilon_1\epsilon_{\text{II}}^2)}{\epsilon_{\text{II}}^3} \frac{l_{\text{TF}}^3}{a^3} \lambda^3 + \mathcal{O}\left(\frac{\lambda^4 l_{\text{TF}}^4}{a^4}\right) \right] \quad (52)$$

$$U_{\text{ext}}^{(1)}(a) = -\frac{Q^2}{16\pi\epsilon_0\epsilon_1 a} \left[1 - \frac{\epsilon_1}{\epsilon_{\text{II}}} \frac{l_{\text{TF}}}{a} + \frac{\epsilon_1^2}{\epsilon_{\text{II}}^2} \frac{l_{\text{TF}}^2}{a^2} - \frac{3(2\epsilon_1^3 - \epsilon_1\epsilon_{\text{II}}^2)}{4\epsilon_{\text{II}}^3} \frac{l_{\text{TF}}^3}{a^3} + \mathcal{O}\left(\frac{l_{\text{TF}}^4}{a^4}\right) \right] \quad (53)$$

which we will show below to exactly match the prediction from the two-body potential imagined as an image multipole series.

A.2 Induced charge potential energy

For the energy of the charge induced in the bounding material, we use the charge-potential relation (7) yielding

$$U_{\text{ind}}^{(1)}(a) = -\pi\epsilon_0\epsilon_{\text{II}}\kappa_{\text{TF}}^2 \int_{-\infty}^0 dz \int_0^{+\infty} dK [\psi_{\text{TF}}(z, K)]^2 K \quad (54)$$

$$U_{\text{ind}}^{(1)}(a) = -\frac{\epsilon_{\text{II}}\kappa_{\text{TF}}^2 Q^2}{4\pi\epsilon_0} \int_{-\infty}^0 dz \int_0^{+\infty} dK \frac{K e^{-2Ka+2\sqrt{K^2+\kappa_{\text{TF}}^2}z}}{(\epsilon_1 K + \epsilon_{\text{II}}\sqrt{K^2+\kappa_{\text{TF}}^2})^2} \quad (55)$$

$$U_{\text{ind}}^{(1)}(a) = -\frac{Q^2}{16\pi\epsilon_0 a} \int_0^{+\infty} d\lambda \frac{2(\kappa_{\text{TF}}a)^2 \lambda e^{-2\lambda}}{\left((\epsilon_1/\epsilon_{\text{II}})\lambda + \sqrt{\lambda^2 + (\kappa_{\text{TF}}a)^2} \right)^2 \sqrt{\lambda^2 + (\kappa_{\text{TF}}a)^2}} \quad (56)$$

$$U_{\text{ind}}^{(1)}(a) = -\frac{Q^2}{16\pi\epsilon_0 a} \mathcal{J}_{\text{ind}}, \quad (57)$$

which vanishes in the limits of ideal metal and ideal dielectric interfaces. This integral can be tabulated as a function of a/l_{TF} or approximated by a rational

function as well. We also provide its expansion in TF length, obtained from the power series of the prefactor of the exponential

$$U_{\text{ind}}^{(1)}(a) = -\frac{Q^2}{8\pi\epsilon_0 a} \int_0^{+\infty} d\lambda \frac{(\kappa_{\text{TF}} a)^2 \lambda e^{-2\lambda}}{\left((\epsilon_{\text{I}}/\epsilon_{\text{II}})\lambda + \sqrt{\lambda^2 + (\kappa_{\text{TF}} a)^2} \right)^2 \sqrt{\lambda^2 + (\kappa_{\text{TF}} a)^2}} \quad (58)$$

$$U_{\text{ind}}^{(1)}(a) = -\frac{Q^2}{8\pi\epsilon_0 a} \int_0^{+\infty} d\lambda e^{-2\lambda} \left[\frac{\lambda}{\kappa_{\text{TF}} a} - \frac{2\epsilon_{\text{I}}}{\epsilon_{\text{II}}} \left(\frac{\lambda}{\kappa_{\text{TF}} a} \right)^2 + \mathcal{O}\left(\left(\frac{\lambda}{\kappa_{\text{TF}} a} \right)^3 \right) \right] \quad (59)$$

$$U_{\text{ind}}^{(1)}(a) = -\frac{Q^2}{16\pi\epsilon_0 a} \left[\frac{l_{\text{TF}}}{2a} - \frac{\epsilon_{\text{I}}}{\epsilon_{\text{II}}} \left(\frac{l_{\text{TF}}}{a} \right)^2 + \mathcal{O}\left(\left(\frac{l_{\text{TF}}}{a} \right)^3 \right) \right], \quad (60)$$

which we use for the comparison with the equivalent contribution to the two-body potential energy in eqn (22).

A.3 Rational function approximation

For simulations, we require fast evaluation of the total one-body energy $U^{(1)}(\mathbf{r}_1) = U_{\text{ext}}^{(1)}(\mathbf{r}_1) + U_{\text{ind}}^{(1)}(\mathbf{r}_1) = -[Q^2/(16\pi\epsilon_0\epsilon_{\text{I}}a)][1 - \mathcal{I}_{\text{ext}} + \epsilon_{\text{I}}\mathcal{I}_{\text{ind}}]$. The integral expression $\mathcal{I}_{\text{ext}} - \epsilon_{\text{I}}\mathcal{I}_{\text{ind}}$ converges to its limiting values linearly in l_{TF} in the ideal metal limit, and linearly in $\kappa_{\text{TF}} = 1/l_{\text{TF}}$ in the ideal dielectric limit, which leads us to propose its approximation in terms of rational functions which interpolate between these two approaches. For the one-body energy, we use

$$U_{\text{apx}}^{(1)}(a) \approx -\frac{Q^2}{16\pi\epsilon_0 a} \times \left[1 - \frac{13.8879(\kappa_{\text{TF}} a)^3 + 37.4625(\kappa_{\text{TF}} a)^2 + 18.6940(\kappa_{\text{TF}} a) + 1}{27.8648(\kappa_{\text{TF}} a)^4 + 73.0987(\kappa_{\text{TF}} a)^3 + 70.3460(\kappa_{\text{TF}} a)^2 + 20.6754(\kappa_{\text{TF}} a) + 1} \right]. \quad (61)$$

This is because the higher order approximations do not yield substantial improvement in precision, as shown in Fig. 7.

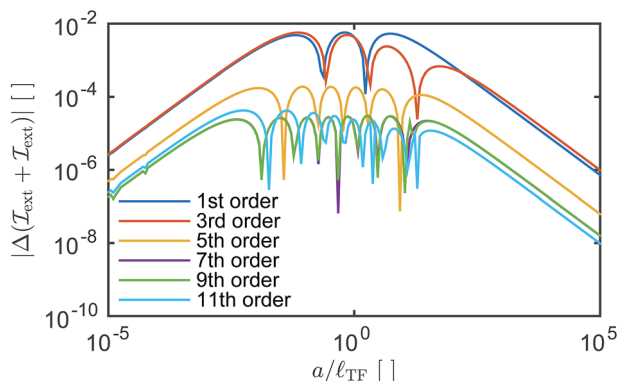


Fig. 7 Absolute error of the rational function approximation of the integral expression $\mathcal{I}_{\text{ext}} - \epsilon_{\text{I}}\mathcal{I}_{\text{ind}} \in [0, 1]$ for increasing orders of approximation.

B Appendix: two-body potential energy

For configurations of charges that do not share the same axis, we cannot represent the energy in terms of an integral purely in the Hankel picture. For example the electrostatic energy of a charge Q_2 at r_2 in the potential ψ of a charge Q_1 at r_1 reads, in general,

$$U^{(2)}(\mathbf{r}_1, \mathbf{r}_2) = Q_2 \int_0^\infty dK J_0(KR) \psi(Q_2, z_2 | z_1, K). \quad (62)$$

This is a function of the distances z_1, z_2 of the two charges from the surface and their mutual distance along it $R = |r_1^{(1)} - r_2^{(1)}|$, and as such involves a larger parameter space than $U^{(1)}$. Moreover, the direct integration is more involved as it includes oscillating terms due to the Bessel function J_0 . In this appendix, we detail approximation schemes for the two contributions $U_{\text{ext}}^{(2)}$ and $U_{\text{ind}}^{(2)}$.

B.1 Multipole expansion

The potential ψ_I outside of an ideal metal, can be found by the image charge method. To generalise it to the case of TF metal, it is instructive to compare the Hankel forms of Green functions, eqn (5) and (6),

potential	ideal metal	ideal dielectric
$\psi_I^>(z > a, K)$	$\frac{Q}{4\pi\epsilon_0\epsilon_I K} e^{-Kz} [e^{+Ka} - e^{-Ka}]$	$\frac{Q}{4\pi\epsilon_0\epsilon_I K} e^{-Kz} \left[e^{+Ka} - \frac{\epsilon_{II} - \epsilon_I}{\epsilon_{II} + \epsilon_I} e^{-Ka} \right]$

$\psi_I^<(z < a, K)$	$\frac{Q}{4\pi\epsilon_0\epsilon_I K} e^{-Ka} [e^{+Kz} - e^{-Kz}]$	$\frac{Q}{4\pi\epsilon_0\epsilon_I K} e^{-Ka} \left[e^{+Kz} - \frac{\epsilon_{II} - \epsilon_I}{\epsilon_{II} + \epsilon_I} e^{-Kz} \right]$
----------------------	--	---

TF metal

$$\frac{Q}{4\pi\epsilon_0\epsilon_I K} e^{-Kz} \left[e^{+Ka} - \frac{\epsilon_{II}\chi_{\text{TF}} - \epsilon_I K}{\epsilon_{II}\chi_{\text{TF}} + \epsilon_I K} e^{-Ka} \right], \quad (64)$$

$$\frac{Q}{4\pi\epsilon_0\epsilon_I K} e^{-Ka} \left[e^{+Kz} - \frac{\epsilon_{II}\chi_{\text{TF}} - \epsilon_I K}{\epsilon_{II}\chi_{\text{TF}} + \epsilon_I K} e^{-Kz} \right]$$

which allows us to identify the second term in the brackets with a generalised image charge potential

$$\psi_{\text{im}}(z, K) = \frac{Q}{4\pi\epsilon_0\epsilon_I K} \frac{\epsilon_I K - \epsilon_{II}\sqrt{K^2 + \kappa_{\text{TF}}^2}}{\epsilon_I K + \epsilon_{II}\sqrt{K^2 + \kappa_{\text{TF}}^2}} e^{-K(a+z)}, \quad (65)$$

which in the case of the dielectric–dielectric interface ($\kappa_{\text{TF}} \rightarrow 0$) corresponds to the well known result of image charge $Q(\epsilon_I - \epsilon_{II})/(\epsilon_I + \epsilon_{II})$ and, for the perfect metal limit, to the image charge $-Q$. Its inverse

$$\psi_{\text{im}}(z, R) = \frac{Q}{4\pi\epsilon_0\epsilon_I} \int_0^\infty dK J_0(KR) \frac{\epsilon_I K - \epsilon_{II}\sqrt{K^2 + \kappa_{\text{TF}}^2}}{\epsilon_I K + \epsilon_{II}\sqrt{K^2 + \kappa_{\text{TF}}^2}} e^{-K(a+z)} \quad (66)$$

is a function of two parameters, which cannot be inverted in terms of analytic functions.

Nevertheless, for a well-defined set of functions we will show that the inversion can be obtained in the form of a series related to the spherical multipole

1 expansion. The key identity is the Hankel transform of powers of K^n with the
 exponential envelope $e^{-K(a+z)}$ expressed in terms of confluent hypergeometric
 functions ${}_2F_1$

$$5 \int_0^\infty dK J_0(KR) K^n e^{-K(a+z)} = \Gamma(n+1)(a+z)^{-(n+1)} {}_2F_1\left(\frac{n+1}{2}, \frac{n+2}{2}; 1; -\left(\frac{R}{a+z}\right)^2\right) \quad (67)$$

which, for n as a positive integer, reduces to functions in the form

$$10 \int_0^\infty dK J_0(KR) K^n e^{-K(a+z)} = \frac{P_n(a+z, R)}{[R^2 + (a+z)^2]^{n+1/2}} \quad (68)$$

where $P_n(a+z, R)$ are polynomials in $(a+z)$ and R , the first few of which are

$$15 P_0(a+z, R) = 1 \quad (69)$$

$$P_1(a+z, R) = a+z \quad (70)$$

$$20 P_2(a+z, R) = -R^2 + 2(a+z)^2 \quad (71)$$

$$P_3(a+z, R) = -9(a+z)R^2 + 6(a+z)^3 \quad (72)$$

$$P_4(a+z, R) = 9R^4 - 72R^2(a+z)^2 + 24(a+z)^4. \quad (73)$$

25 Using this knowledge we can now expand the integrand in eqn (66) in powers
 of $l_{TF} = \kappa_{TF}^{-1}$,

$$30 \frac{\varepsilon_I/\varepsilon_{II} - \sqrt{1 + (\kappa_{TF}/K)^2}}{\varepsilon_I/\varepsilon_{II} + \sqrt{1 + (\kappa_{TF}/K)^2}} = -1 + \frac{2\varepsilon_I}{\varepsilon_{II}\kappa_{TF}}K - \frac{2\varepsilon_I^2}{(\varepsilon_{II}\kappa_{TF})^2}K^2 + \frac{2\varepsilon_I^3 - \varepsilon_I\varepsilon_{II}^2}{(\varepsilon_{II}\kappa_{TF})^3}K^3 \\ + \mathcal{O}\left(\frac{K^4}{\kappa_{TF}^4}\right), \quad (74)$$

and obtain a series for the generalised image potential

$$35 \psi_{im}(z, R) = \frac{Q}{4\pi\varepsilon_0\varepsilon_I} - \left[\frac{1}{[R^2 + (a+z)^2]^{1/2}} + \frac{2\varepsilon_I}{\varepsilon_{II}\kappa_{TF}} \frac{a+z}{[R^2 + (a+z)^2]^{3/2}} \right. \\ 40 + \frac{2\varepsilon_I^2}{(\varepsilon_{II}\kappa_{TF})^2} \frac{R^2 - 2(a+z)^2}{[R^2 + (a+z)^2]^{5/2}} - \frac{2\varepsilon_I^3 - \varepsilon_I\varepsilon_{II}^2}{(\varepsilon_{II}\kappa_{TF})^3} \frac{9(a+z)R^2 - 6(a+z)^3}{[R^2 + (a+z)^2]^{7/2}} \\ \left. + \mathcal{O}\left(\frac{R^4}{\kappa_{TF}^4 [R^2 + (a+z)^2]^{9/2}}\right) \right]. \quad (75)$$

The first term can be identified with the $-Q$ ideal metal image charge. We
 rewrite the series using that the distance from the ideal image charge position
 50 reads $r = [R^2 + (a+z)^2]^{1/2}$ and the related angle ϕ from the z -axis, where $\cos \phi = (z+a)/r$. The potential transformed to these variables reads

$$\psi_{\text{im}}(z, R) = \frac{Q}{4\pi\epsilon_0\epsilon_{\text{I}}} \left[-\frac{1}{r} + \frac{2\epsilon_{\text{I}}}{\epsilon_{\text{II}}\kappa_{\text{TF}}} \frac{\cos\phi}{r^2} - \frac{2\epsilon_{\text{I}}^2}{(\epsilon_{\text{II}}\kappa_{\text{TF}})^2} \frac{3\cos^2\phi - 1}{r^3} + \frac{3(2\epsilon_{\text{I}}^3 - \epsilon_{\text{I}}\epsilon_{\text{II}}^2)}{(\epsilon_{\text{II}}\kappa_{\text{TF}})^3} \frac{5\cos^3\phi - 3\cos\phi}{r^4} + \mathcal{O}\left(\frac{1}{\kappa_{\text{TF}}^4 r^5}\right) \right], \quad (76)$$

resulting in eqn (16) of the main text. The terms correspond to the potentials of point charge $-Q$, a dipole $2Q\epsilon_{\text{I}}l_{\text{TF}}\hat{z}/\epsilon_{\text{II}}$ oriented along the z -axis, a $\hat{z}\hat{z}$ -quadrupole $2Q\epsilon_{\text{I}}^2l_{\text{TF}}^2/\epsilon_{\text{II}}^2$, and a $\hat{z}\hat{z}\hat{z}$ -octupole $3Q(2\epsilon_{\text{I}}^3 - \epsilon_{\text{I}}\epsilon_{\text{II}}^2)l_{\text{TF}}^3/\epsilon_{\text{II}}^3$, etc. The derivation of higher order terms is thus simplified even further, as the polynomials (70–74) are revealed to be closely related to Legendre polynomials of $\cos\psi$ by the transformation to angular variables and expressing all sines in terms of cosines. The shape of the potential is then given by the corresponding spherical harmonics Y_n^0 which are also the only ones allowed by the cylindrical symmetry around the z -axis. It also matches the expansion in eqn (53) where the self-energy is obtained as $U_{\text{ext}} = Q\psi_{\text{im}}/2$ for $r = a$ and $\cos\psi = 1$.

B.2 Rational function approximation of $U_{\text{ind}}^{(2)}$

The final expression (23) for the “induced charge” part of the two-body energy is given in terms of an integral of elliptic integrals. While rapidly convergent, the evaluation of this integral is numerically costly. For numerical applications, we remark that by definition it is a function of d and $(a + b)$, exclusively,

$$U_{\text{TF}}(\mathbf{r}_1, \mathbf{r}_2) \simeq -\frac{Q_1 Q_2 l_{\text{TF}}}{4\pi\epsilon_0} \times \frac{1}{\pi} \times \frac{6.3794d^2(a+b) + 5.0213(a+b)^3}{d^5 + 0.218699d^4(a+b) + 1.38638d^3(a+b)^2 + 1.71388d^2(a+b)^3 + 0.820837(a+b)^5}. \quad (77)$$

For most practical purposes, this approximation results in a smaller error than the initial expansion in l_{TF} , whose relative error scales linearly with a/l_{TF} , and b/l_{TF} , approximately as ϵ ; $2a/l_{\text{TF}}$. This limits the closest approach to the TF metal boundary for this expression. For $l_{\text{TF}} = 0.5 \text{ \AA}$ and therefore $a > 1 \text{ \AA}$ for an error of about 10 percent. Note, that the term that we are approximating is already an order of l_{TF} lower than the leading term in $U_{\text{ind}}^{(2)}$, therefore its error is of proportionally lower importance.

Acknowledgements

We thank B. Rotenberg and E. Charlaix for many fruitful discussions. J. C., A. N. and A. S. acknowledge funding from the European Union’s H2020 Framework Programme/ERC Starting Grant agreement number 637748 – NanoSOFT. L. B. acknowledges support from the European Union’s FP7 Framework Programme/ERC Advanced Grant Micromegas. The authors acknowledge funding from ANR project BlueEnergy.

References

- 1 M. V. Fedorov and A. A. Kornyshev, Ionic liquids at electrified interfaces, *Chem. Rev.*, 2014, **114**, 2978–3036.

- 1 2 E. Uesugi, H. Goto, R. Eguchi, A. Fujiwara and Y. Kubozono, Electric double-layer capacitance between an ionic liquid and few-layer graphene, *Sci. Rep.*, 2013, **3**, 1595.
- 3 M. Palacio and B. Bhushan, A review of ionic liquids for green molecular lubrication in nanotechnology, *Tribol. Lett.*, 2010, **40**(2), 247–268.
- 5 4 C. Dold, T. Amann and A. Kailer, Influence of electric potentials on friction of sliding contacts lubricated by an ionic liquid, *Phys. Chem. Chem. Phys.*, 2015, **17**(16), 10339–10342.
- 10 5 B. Rotenberg and M. Salanne, Structural Transitions at Ionic Liquids Interfaces, *J. Phys. Chem. Lett.*, 2015, **6**(24), 4978–4985.
- 6 S. Bovio, A. Podesta, C. Lenardi and P. Milani, Evidence of extended solidlike layering in [Bmim][NTf₂] ionic liquid thin films at room-temperature, *J. Phys. Chem. B*, 2009, **113**(19), 6600–6603.
- 15 7 I. Bou-Malham and L. Bureau, Nanoconfined ionic liquids: effect of surface charges on flow and molecular layering, *Soft Matter*, 2010, **6**(17), 4062–4065.
- 8 Y. Yokota, T. Harada and K. I. Fukui, Direct observation of layered structures at ionic liquid/solid interfaces by using frequency-modulation atomic force microscopy, *Chem. Commun.*, 2010, **46**(45), 8627–8629.
- 20 9 A. M. Smith, K. R. J. Lovelock, N. N. Gosvami, T. Welton and S. Perkin, Quantized friction across ionic liquid thin films, *Phys. Chem. Chem. Phys.*, 2013, **15**(37), 15317–15320.
- 25 10 M. A. Gebbie, A. M. Smith, H. A. Dobbs, A. A. Lee, G. G. Warr, X. Banquy, M. Valtiner, M. W. Rutland, J. N. Israelachvili, S. Perkin and R. Atkin, Long range electrostatic forces in ionic liquids, *Chem. Commun.*, 2017, **53**, 1214–1224.
- 11 J. Comtet, A. Niguès, V. Kaiser, L. Bocquet and A. Siria, Nanoscale capillary freezing of ionic liquids confined between metallic interfaces and the role of electronic screening, arXiv:1611.08448 [cond-mat], 2016.
- 30 12 S. Bovio, A. Podestà, P. Milani, P. Ballone and M. G. Del Pòpolo, Nanometric ionic-liquid films on silica: a joint experimental and computational study, *J. Phys.: Condens. Matter*, 2009, **21**(42), 424118.
- 13 C. Merlet, B. Rotenberg, P. A. Madden, P.-L. Taberna, P. Simon, Y. Gogotsi and M. Salanne, On the molecular origin of supercapacitance in nanoporous carbon electrodes, *Nat. Mater.*, 2012, **11**(4), 306–310.
- 35 14 S. Kondrat and A. Kornyshev, Charging dynamics and optimization of nanoporous supercapacitors, *J. Phys. Chem. C*, 2013, **117**(24), 12399–12406.
- 15 S. Kondrat, P. Wu, R. Qiao and A. Kornyshev, Accelerating charging dynamics in subnanometre pores, *Nat. Mater.*, 2014, **13**, 387–393.
- 40 16 C. C. Rochester, A. A. Lee, G. Pruessner and A. A. Kornyshev, Interionic interactions in conducting nanoconfinement, *ChemPhysChem*, 2013, **14**(18), 4121–4125.
- 17 A. A. Lee, S. Kondrat, and A. A. Kornyshev. Single-file charge storage in conducting nanopores. *Phys. Rev. Lett.*, **113**(4):048701 2014.
- 45 18 G. D. Mahan, *Many-Particle Physics*, Springer Science & Business Media, 2000.
- 19 M. Vorotyntsev and A. A. Kornyshev, Electrostatic interaction on a metal/insulator interface, *Zh. Eksp. Teor. Fiz.*, 1980, **78**(3), 1008–1019.
- 20 A. A. Kornyshev and M. A. Vorotyntsev, Nonlocal electrostatic approach to the double layer and adsorption at the electrode–electrolyte interface, *Surf. Sci.*, 1980, **101**(1–3), 23–48.

- 1 21 A. A. Kornyshev, W. Schmickler and M. A. Vorotyntsev, Nonlocal electrostatic approach to the problem of a double layer at a metal–electrolyte interface, *Phys. Rev. B: Condens. Matter Mater. Phys.*, 1982, **25**(8), 5244–5256.
- 5 22 J. S. Rowlinson and B. Widom, *Molecular Theory of Capillarity*, Oxford University Press, Oxford, 1989.
- 23 J. D. Jackson, *Classical Electrodynamics*, Wiley, New York, 3th edn, 1998.
- 24 J. Ilja Siepman and M. Sprik, Influence of surface topology and electrostatic potential on water/electrode systems, *J. Chem. Phys.*, 1995, **102**(1), 511–524.
- 10 25 S. Tyagi, A. Arnold and C. Holm, Electrostatic layer correction with image charges: a linear scaling method to treat slab 2D+h systems with dielectric interfaces, *J. Chem. Phys.*, 2008, **129**(20), 204102.
- 26 T. R. Gingrich and M. Wilson, On the ewald summation of Gaussian charges for the simulation of metallic surfaces, *Chem. Phys. Lett.*, 2010, **500**(1–3), 178–183.
- 15 27 N. D. Lang and W. Kohn, Theory of metal surfaces: induced surface charge and image potential, *Phys. Rev. B: Solid State*, 1973, **7**(8), 3541–3550.
- 28 F. W. J. Olver, D. W. Lozier, R. F. Boisvert and C. W. Clark, *NIST Handbook of Mathematical Functions*, Cambridge University Press, 2010.
- 20 29 M. Bezerra, R. de Melo e Souza, W. J. M. Kort-Kamp and C. Farina Subtleties in obtaining the electrostatic energy of continuous distributions. *Eur. J. Phys.*, **35**(6):065021 (2014).
- 30 P. P. Ewald, Die Berechnung Optischer und Elektrostatisher Gitterpotentiale, *Ann. Phys.*, 1921, **369**(3), 253–287.
- 25 31 S. W. de Leeuw, J. W. Perram and E. R. Smith, Simulation of electrostatic systems in periodic boundary conditions. I. Lattice sums and dielectric constants, *Proceedings of the Royal Society A: Mathematical, Physical and Engineering Sciences*, 1980, **373**(1752), 27–56.
- 32 J. N. Israelachvili, *Intermolecular and Surface Forces*, Academic Press, Burlington, MA, 3rd edn, 2011.
- 30 33 M. Tariq, M. G. Freire, B. Saramago, J. A. P. Coutinho, J. N. Canongia Lopes and L. P. N. Rebelo, Surface tension of ionic liquids and ionic liquid solutions, *Chem. Soc. Rev.*, 2012, **2**, 829–868.
- 35 34 L. Bocquet and E. Charlaix, Nanofluidics, from bulk to interfaces, *Chem. Soc. Rev.*, 2010, **39**(3), 1073–1095.
- 35 35 E. Secchi, S. Marbach, A. Niguès, D. Stein, A. Siria and L. Bocquet, Massive radius-dependent flow slippage in single carbon nanotubes, *Nature*, 2016, **537**(7619), 210–213.
- 40 36 J. Köfinger, G. Hummer and C. Dellago, Single-file water in nanopores, *Phys. Chem. Chem. Phys.*, 2011, **13**(34), 15403.
- 37 G. Algara-Siller, O. Lehtinen, F. C. Wang, R. R. Nair, U. Kaiser, H. A. Wu, A. K. Geim and I. V. Grigorieva, Square ice in graphene nanocapillaries, *Nature*, 2015, **519**(7544), 443–445.
- 45 38 K. V. Agrawal, S. Shimizu, L. W. Drahushuk, D. Kilcoyne and M. S. Strano, Observation of extreme phase transition temperatures of water confined inside isolated carbon nanotubes, *Nat. Nanotechnol.*, 2016, advance online publication.
- 50 39 L. Onsager and Samaras, The surface tension of Debye–Hückel electrolytes, *J. Chem. Phys.*, 1934, **2**, 528–536.

- 1 40 G. Tocci, L. Joly and A. Michaelides, Friction of Water on Graphene and
Hexagonal Boron Nitride from *Ab Initio* Methods: Very Different Slippage
Despite Very Similar Interface Structures, *Nano Lett.*, 2014, **14**, 6872–6877.
- 5 41 B. Grosjean, C. Péan, A. Siria, L. Bocquet, R. Vuilleumier and M.-L. Bocquet,
Chemisorption of Hydroxide on 2D Materials From DFT Calculations:
Graphene *Versus* Hexagonal Boron Nitride, *J. Phys. Chem. Lett.*, 2016, **7**,
4695–4700.
- 10 42 A. Siria, P. Poncharal, A.-L. Biance, R. Fulcrand, X. Blase, S. Purcell and
L. Bocquet, Giant osmotic energy conversion measured in a single
transmembrane boron-nitride nanotube, *Nature*, 2013, **494**, 455–458.
- 43 A. A. Kornyshev, A. I. Rubinshtein and M. A. Vorotyntsev, Image potential near
a dielectric/plasma like medium interface, *Phys. Status Solidi B*, 1977, **84**(7619),
125–132.
- 15 44 A. A. Kornyshev and M. A. Vorotyntsev, Analytic expression for the potential of
a test charge in a dielectric bounded by solid state plasma, *J. Phys. C: Solid
State Phys.*, 1978, **11**, L691–L694.
- 45 A. A. Kornyshev and W. Schmickler, On the coverage dependence of the partial
charge transfer coefficient, *J. Electroanal. Chem.*, 1986, **202**, 1–21.
- 20 46 M. A. Vorotyntsev and S. N. Ivanov, Statistical Mechanics of an Ionic Ensemble
Adsorbed at the Metal–Dielectric Interface, *Soviet Physics–JETP*, 1985, **61**, 1028–
1032.
- 47 M. A. Vorotyntsev, Attraction Constant of the Ionic Adsorption Isotherm at an
Uniform Metal–Electrolyte Solution Interface, *Sov. Electrochem.*, 1985, **21**, 257–
259.
- 25 48 J. C. Inkson, Many-body effect at metal-semiconductor junctions. II. The self
energy and band structure distortion, *J. Phys. C: Solid State Phys.*, 1973, **6**,
1350–1362.
- 49 J. Heinrichs, Response of metal surfaces to static and moving point charges
and to polarizable charge distributions, *Phys. Rev. B: Solid State*, 1973, **8**(4),
1346–1364.
- 30 50 D. M. Newns, Fermi–Thomas Response of a Metal Surface to an External Point
Charge, *J. Chem. Phys.*, 1969, **10**, 1613–1629.
- 35 51 M. A. Vorotyntsev, A. A. Kornyshev and A. I. Rubinshtein, Electrostatic
interaction of ions in solution at the surface of an electrode: penetration of
the ion field into the electrode, *Dokl. Phys.*, 1979, **24**, 848–850.
- 40
- 45
- 50